

REPORT DOCUMENTATION PAGE			Form Approved OMB NO. 0704-0188		
<p>The public reporting burden for this collection of information is estimated to average 1 hour per response, including the time for reviewing instructions, searching existing data sources, gathering and maintaining the data needed, and completing and reviewing the collection of information. Send comments regarding this burden estimate or any other aspect of this collection of information, including suggestions for reducing this burden, to Washington Headquarters Services, Directorate for Information Operations and Reports, 1215 Jefferson Davis Highway, Suite 1204, Arlington VA, 22202-4302. Respondents should be aware that notwithstanding any other provision of law, no person shall be subject to any penalty for failing to comply with a collection of information if it does not display a currently valid OMB control number.</p> <p>PLEASE DO NOT RETURN YOUR FORM TO THE ABOVE ADDRESS.</p>					
1. REPORT DATE (DD-MM-YYYY) 02-02-2010		2. REPORT TYPE Final Report		3. DATES COVERED (From - To) 1-May-2004 - 31-Oct-2009	
4. TITLE AND SUBTITLE Design and Processing of Electret Structures - FINAL REPORT			5a. CONTRACT NUMBER W911NF-04-1-0170		
			5b. GRANT NUMBER		
			5c. PROGRAM ELEMENT NUMBER 611103		
6. AUTHORS George M. Whitesides, Zhigang Suo, Mara Prentiss, Ilhan Aksay, Roberto Car			5d. PROJECT NUMBER		
			5e. TASK NUMBER		
			5f. WORK UNIT NUMBER		
7. PERFORMING ORGANIZATION NAMES AND ADDRESSES Harvard University Office of Sponsored Research 1350 Massachusetts Ave. Holyoke 727 Cambridge, MA 02138 -			8. PERFORMING ORGANIZATION REPORT NUMBER		
9. SPONSORING/MONITORING AGENCY NAME(S) AND ADDRESS(ES) U.S. Army Research Office P.O. Box 12211 Research Triangle Park, NC 27709-2211			10. SPONSOR/MONITOR'S ACRONYM(S) ARO		
			11. SPONSOR/MONITOR'S REPORT NUMBER(S) 46649-MS-MUR.8		
12. DISTRIBUTION AVAILABILITY STATEMENT Approved for Public Release; Distribution Unlimited					
13. SUPPLEMENTARY NOTES The views, opinions and/or findings contained in this report are those of the author(s) and should not be construed as an official Department of the Army position, policy or decision, unless so designated by other documentation.					
14. ABSTRACT Our final report on this very successful project summarizes the accomplishments of this MURI. The team was lead by the Whitesides group, and included two other groups from Harvard University, and the Aksay group at Princeton University. The original objectives of this research program were to: (i) understand the nature of the charge resulting from					
15. SUBJECT TERMS Electrets, electrostatics, self-assembly, galvanography, electrohydrodynamic printing, surfactant aggregates, guided growth, contact charge separation					
16. SECURITY CLASSIFICATION OF:			17. LIMITATION OF ABSTRACT UU	15. NUMBER OF PAGES	19a. NAME OF RESPONSIBLE PERSON George Whitesides
a. REPORT UU	b. ABSTRACT UU	c. THIS PAGE UU			19b. TELEPHONE NUMBER 617-495-9430

FINAL REPORT

DESIGN AND PROCESSING OF ELECTRET STRUCTURES

W911NF-04-1-0170

Principal Investigator:

George M. Whitesides
Department of Chemistry and Chemical Biology
Harvard University
Cambridge, Massachusetts 02138
Telephone: (617) 495-9430
Facsimile: (617) 495-9857
e-mail: gwhitesides@gmwgroup.harvard.edu

Subaward Principal Investigator:

Ilhan A. Aksay
Department of Chemical Engineering
Princeton University
Princeton, New Jersey 08540
Telephone: (609) 258-4393
Facsimile: (609) 258-6835
e-mail: iaksay@princeton.edu

Award period: 1st May 2004 – 31st October 2009

Whitesides Group – Harvard University**OBJECTIVES**

The objectives of this research program were to: (i) understand the nature of the charge resulting from contact electrification, (ii) understand the mechanisms and fundamental limits of tribocharging, (iii) develop new materials. Specifically, the goals were to establish what determine the rate of electrostatic charging and discharging in solid electrets, to understand the process by which charge transfer occurs and to explore self-assembly based on electrostatic interactions.

ACCOMPLISHMENTS**1. Ionic Electrets**

1.1 Preparation of Ionic Electrets. We developed a method of making ionic electrets from monodisperse polystyrene microspheres (electrets whose charge comes from an imbalance of ions, rather than from the transfer of electrons). Our method of preparing ionic electrets involves fixing charges of one sign (for example, sulfonate groups, $-\text{SO}_3^-$) and mobile ions of the opposite sign (for example, Na^+).

We also succeeded in fabricating ionic electrets from monodisperse glass microspheres. We silanized glass beads using commercially available, charged alkylsiloxanes. In addition to the glass microspheres, we have patterned ionic electrets onto planar silicon wafers (with thermal oxide layers) by microcontact printing (**Figure 1**).

Using these ionic electrets, we found that the dielectric breakdown of the surrounding medium imposes a limit on the maximum charge that an electret can have.

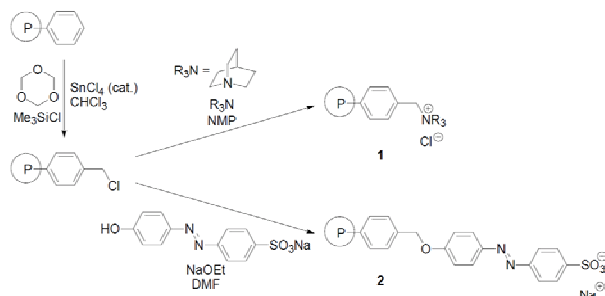


Figure 1. A scheme showing chemical modification of crosslinked polystyrene microspheres to yield spheres with tetraalkylammonium (**1**) and sulfonate (**2**) functional groups

1.2 Development of Tools for Studying Ionic Electrets. We developed several tools for studying microsphere-based ionic electrets. **Figure 2** shows the basic designs of two of these tools. The first tool features a central polyethylene tube, and three outer concentric tubes made of aluminum; each tube is individually connected to the positive, negative, and ground terminals of an electrometer. The electrometer measures the net charge of the microsphere that is in the polyethylene tube. We have used the straight tool (**Figure 2a**) to measure the magnitude and sign of charge of microspheres after contact electrification. We used the looped tool (**Figure 2b**) to measure the kinetics of charging of individual microspheres as they continuously collided with the polyethylene tube.

DESIGN AND PROCESSING OF ELECTRET STRUCTURES

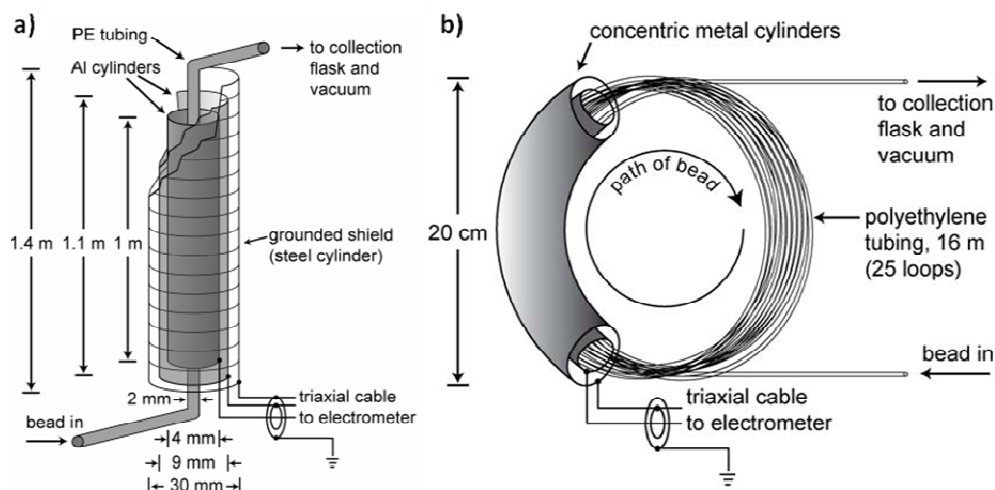


Figure 2. (a) Schematic illustration of the apparatus developed for measuring the charge on individual microspheres. (b) A schematic representation of the tool used to measure repeatedly the accumulation of charge on a single bead.

2. Observation of Dynamics of Charging and Discharging induced by Contact Electrification

We used a tool that we had developed in our lab previously, which we called the “Rolling Sphere Tool” (RST) (**Figure 3**), to understand the dynamics of contact charging and discharging. The RST consisted of a steel sphere rolling on an organic insulating surface under the influence of a rotating magnet below the organic insulator. An electrode located directly beneath the insulator surface measured the charge of the system. We obtained real time kinetics of contact electrification using the RST tool. There are two kinetically distinct processes: 1) charging at a constant rate; 2) abrupt discharging, when the potential difference between sphere and surface reaches a critical value determined by the dielectric strength of air.

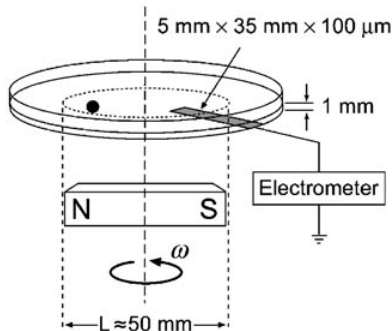


Figure 3. A schematic representation of the Rolling Sphere Tool” (RST) that measures the separation of charge by contact electrification between a rolling metal bead and a polymer.

3. Determination of the Location of Electrical Discharge Events

We developed a method for determining the precise location of an electrical discharge using the RST. The raw data obtained from a sphere rolling on an organic insulator surface indicates where a discharge between the sphere and the organic insulating surface occurred. The method works for both metal/insulator and insulator/insulator interactions. Using this method to track where discharges occurred we evaluated the propensity for discharge to take place on surfaces functionalized with regions of different materials (**Figure 4**).

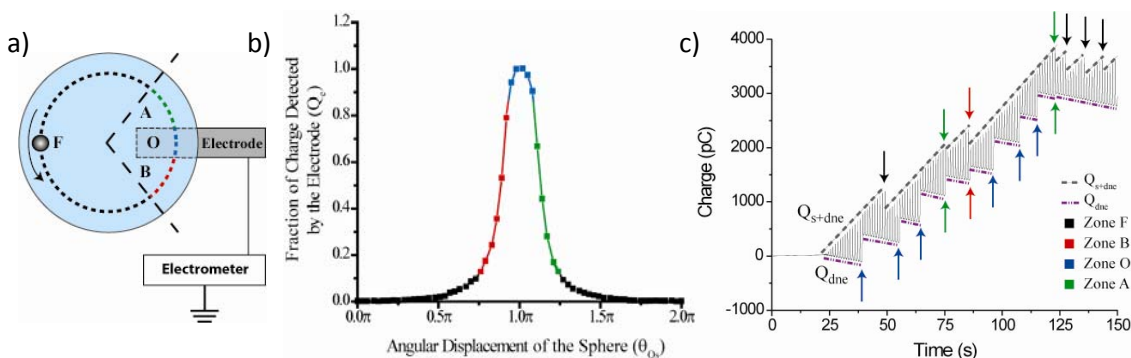


Figure 4. a) The circular path of sphere can be divided into detection zones each of which describes the relationship between the charge on the sphere that the electrode sensed and the position of the sphere *wrt* the electrode. (Zone **F** – the sphere is *far* from the electrode; Zone **B** – the sphere is near the electrode, approaching it (*before* the electrode); Zone **O** – the sphere is directly *over* the electrode; Zone **A** – the sphere is near the electrode, moving away from it (*after* the electrode)). b) A single revolution of the sphere highlighting the fraction of charge that the electrode detected (black: 0-0.1, red and green: 0.1-0.9, blue: 0.9-1.0) at each position of the sphere *wrt* the electrode (width, $w = 1.0$ cm); c) The shape of the data around each discontinuity in the unprocessed data indicates the position of that discharge.

4. Rationally Designed, Functional Electrets

Using our solid mechanistic understanding of contact electrification (the transfer of ions between surfaces causes the accumulation of electrical potential) we rationally designed materials that displayed two different characteristic charging behaviors: i) we fabricated surfaces patterned with positively and negatively charging functional groups to generate surfaces that resisted developing a net charge by contact electrification; ii) we fabricated a material that switches the sign of charge it acquires upon contact electrification after irradiation with UV light (**Figure 5**).

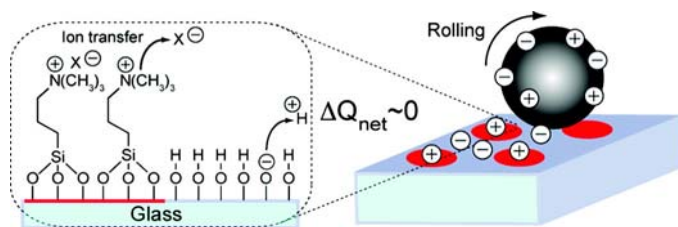


Figure 5. A sphere that rolls on a surface patterned with both positively and negatively charging functional group does not develop a net charge because equal amounts of positive and negative charges are transferred to the sphere.

5. Self-Assembly

5.1 Directed Self-Assembly. We demonstrated the use of electrostatic charging to place small components in predetermined positions by utilizing a patterned electrode on a dielectric substrate. The dielectric support (typically polystyrene) is sandwiched in between an upper electrode (gold, with holes opened in it), and a continuous bottom electrode. When a suitable electric field is applied between these electrodes across the dielectric support, dielectric spheres (e.g., glass) position themselves on the open windows of the upper electrode.

5.2 Electrostatic Self-Assembly of Polystyrene Microspheres. Based on our method to fabricate chemically modified polystyrene microspheres, we demonstrated the self-assembly of three-dimensional microstructures by contact electrification. We predictably and rationally controlled the contact electrification of polystyrene microspheres, and used the resulting charged materials for electrostatic self-assembly. We controlled the contact electrification of the microspheres by introducing immobilized ions and mobile counter ions; the choice of these ions determined the electrostatic charges that these beads

DESIGN AND PROCESSING OF ELECTRET STRUCTURES

acquired through contact before and during the assembly process. Oppositely charged microspheres assembled into uniform spherical microstructures under the influence of electrostatic forces (**Figure 6**).

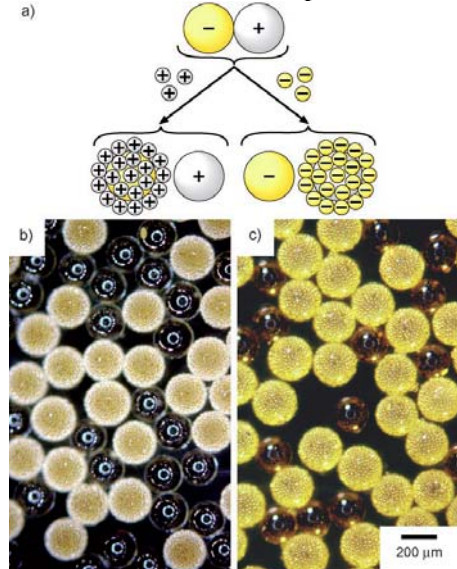


Figure 6. a) A schematic representation of the experiment demonstrating that assembly involves electrostatic interactions. b) An optical micrograph of the assemblies resulting from a mixture of 200-μm-diameter positively charged colorless spheres, 200-μm-diameter negatively charged orange spheres, and 20-μm-diameter positively charged colorless spheres. c) An optical micrograph (on the same scale) of the assemblies resulting from a mixture of 200-μm-diameter positively charged colorless spheres, 200-μm-diameter negatively charged orange spheres, and 20-μm-diameter negatively charged orange spheres.

5.3 Electrostatic Self-Assembly of mm-Sized Beads. Using electrostatic interactions among polymeric materials, we constructed a physical model for the study of folding of polymers in two dimensions. The model that we developed is based on the simplest theoretical model for polymers—the “beads-on-a-string” model. Using this model we demonstrated the folding of short sequences loosely analogous to palindromic sequences of RNA and folding with length scales that correspond realistically to polymers (e.g. polynucleic acids, **Figure 7**).

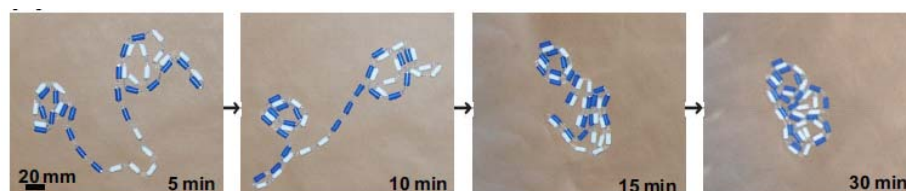


Figure 7. Time-lapse photographs capture the folding process of a sequence of 40 cylindrical beads.

In addition, we demonstrated the formation of 2D Coulombic crystals from millimeter-sized spheres (Teflon and Nylon spheres), and the separation of these crystals from gold-coated spheres. The formation of a Coulombic crystal, and the separation of this crystal from the disordered gold-coated particles can serve as a simple, physical model for the nucleation of a molecular crystal in a polarizable solvent (**Figure 8**).

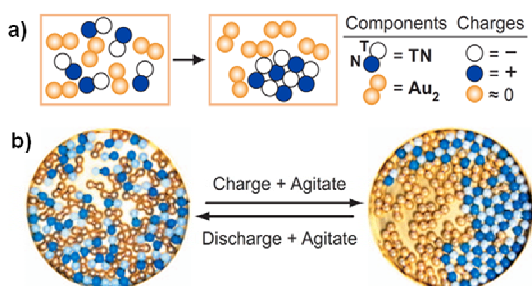


Figure 8. a) A schematic illustration of the experimental design: the blue particles are Nylon (N) spheres, the white are Teflon (T) and the yellow are gold-coated (Au). The TN particles have dipoles formed by a negatively charged sphere T and a positively charged sphere N. These particles interact more strongly with each other than they do with the less-charged particles of Au_2 gold, and form a crystal that excludes Au_2 . b) Photographs of TN and Au_2 particles within a circular frame.

Suo Group - Harvard University

This project has been exceptionally satisfying for us. Two PhD students partially supported by this project have graduated, and have gone to Iowa State University and Duke University as assistant professor. A postdoc supported by this project is now assistant professor at Georgia Tech.

We have focused on developing the mechanics of electroactive polymers. Two difficulties have long troubled the field theory of dielectric solids. First, when two electric charges are placed inside a dielectric solid, the force between them is not a measurable quantity. Second, when a dielectric solid deforms, the true electric field and true electric displacement are not work conjugates. These difficulties are circumvented in a new formulation of the theory. The approach does not start with Newton's laws of mechanics and Maxwell-Faraday theory of electrostatics, but produces them as consequences. The definitions lead to familiar and decoupled field equations. Electromechanical coupling enters the theory through material laws. In the limiting case of a fluid dielectric, the theory recovers the Maxwell stress. The approach is developed for finite deformation, and is applicable to both elastic and inelastic dielectrics. As applications of the theory, we discuss material laws for elastic dielectrics, and study infinitesimal fields superimposed upon a given field, including phenomena such as vibration, wave propagation, and bifurcation.

A recent experiment has shown that the homogeneous deformation of the layer can be unstable, giving way to an inhomogeneous deformation, such that regions of two kinds coexist in the layer, one being flat and the other wrinkled. To analyze this instability, we construct for a class of model materials, which we call ideal dielectric elastomers, a free-energy function comprising contributions from stretching and polarizing. We show that the free-energy function is typically non-convex, causing the elastomer to undergo a discontinuous transition from a thick state to a thin state. When the two states coexist in the elastomer, a region of the thin state has a large area, and wrinkles when constrained by nearby regions of the thick state. We show that an elastomer described by the Gaussian statistics cannot stabilize the thin state, but a stiffening elastomer near the extension limit can. We further show that the instability can be tuned by the density of cross links and the state of stress.

Mechanical energy can be converted to electrical energy by using a dielectric elastomer generator. The elastomer is susceptible to various modes of failure, including electrical breakdown, electromechanical instability, loss of tension, and rupture by stretch. The modes of failure define a cycle of maximal energy that can be converted. This cycle is represented on planes of work-conjugate coordinates, and may be used to guide the design of practical cycles.

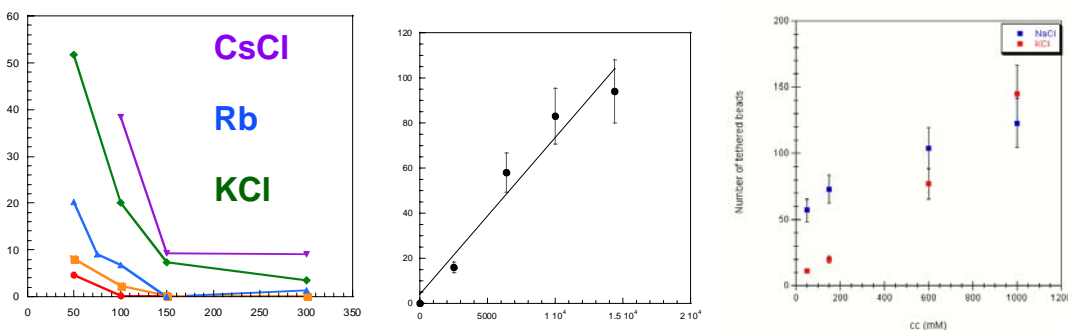
More recently we have focused on the effects of electric charge on the deformation of soft materials. Examples include dielectric elastomers and polyelectrolyte gels. We have developed nonlinear field theories, and implement computational methods. In particular, we show that the Maxwell stress is a consequence of a very special material model, and have extended the idea to more general material models. As an application of the theory, we studied electromechanical instability in dielectric elastomers.

Prentiss Group - Harvard University

Large scale electrets are rare because electrical forces are so large that macroscopic structures are almost always almost electrically neutral. In contrast, objects with sizes of the order of a micron and below are often permanently charged. For example, the unscreened electric field 4 nm from a double stranded DNA molecule (dsDNA) is 5×10^7 V/m. As our part of the electret project, we investigated the interactions between the highly charge phosphate backbones of DNA molecules in solutions containing various concentrations of ions.

Coulombic forces play a strong role in interactions at this size scale, and are believed to make a significant contribution to the self-assembly of complex structures. The Whitesides group has done extensive work on protein interactions and the role that charge plays in those systems. We focused on the interaction between the charged phosphate backbones of one single double stranded DNA molecule, as well as the recognition process that allows two sequence matched dsDNA strands to find their sequence matched pair will rejecting mismatched sequences that may still have a substantial overlap in short regions. The latter is an example of a system where “nanobar code” based recognition drives correct self-assembly. In our theoretical study of this system, we also arrived at some basic principles of bar code based recognition that we verified in collaboration with the Whitesides group where the principles were tested on cm sized objects which underwent electret based self-assembly into more complex structures.

In our early experiments, we measured the charge screening between the two phosphate backbones, where the separation between the backbones is approximately 2.3 nm. Below is a plot of the hysteresis measured for extension vs force curves for double stranded dsDNA. If the hysteresis value is low, the repulsion between the phosphate backbones is well screened, but if the hysteresis is high the repulsion is poorly screened. The results are shown in the figure on the left below. The figure shows that different monovalent salts screen differently, so simply theories based on ionic strength will not describe the Coulombic interactions at the nm scale well. In addition, the screening does not simply scale with mass, as one would expect if it were a charge density effect. Finally, we see that changing the anion alters the result, indicating that one cannot simply consider the screening of the phosphates by the cations, but one must include additional interactions between the ions and the water.



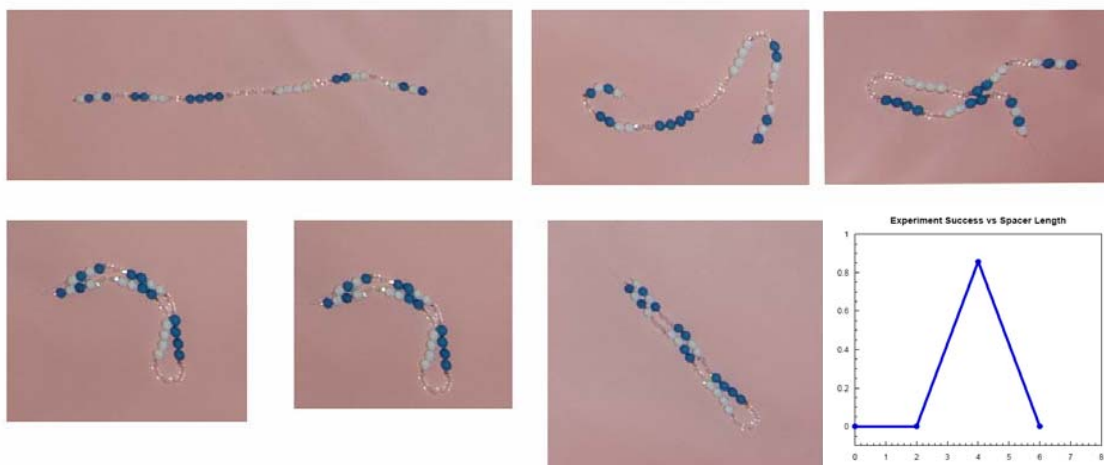
In later experiments, we focused on nano-bar code based recognition between two double stranded dsDNA molecules. This was believed to be an electret effect, but the final results of our research suggest that the Coulombic effects may be less important the hydration effects where the local structure of water plays an important role. The local structuring of water at surfaces was studied by the Carr group.

In our group we produced the first experimental demonstration that pair-wise sequenced based recognition between two intact dsDNA molecules is possible in the absence of proteins, where some results are shown in the central and right hand panels above. The number of correctly paired molecules as a function of the square of the molecule concentration is shown in the central figure, which increases linearly suggesting that the sequence identification is a pairwise process. The pairing as a function of salt concentration for NaCl and KCl is shown in the right hand figure. The pairing increases with increasing salt concentration for both salts, but NaCl screens far more effectively at low concentrations than KCl, though there may be a reversal of effectiveness at higher salt concentrations. The low concentration

screening difference between NaCl and KCl is consistent with the earlier screening results shown in the left hand panel.

Finally, we studied the generalized problem of bar-code based self-assembly and in collaboration with the Whitesides group showed that this understanding could be exploited to do macroscopic electret based self-assembly. We demonstrated theoretically that any bar code based self-assembly system will get eternally trapped in false minima if the length of the bar code is increased too much. For systems that use positive and negative charge, extending beyond 10 bits is extremely difficult if all bits interact at once, as they do if the bar code is rigid. In contrast, if the bar code is flexible so that only a few bits interact at a time, then the problem of false minima is greatly reduced; however, correct matches need to fully pair, so there must be a connection between the short regions that initially interact and the rest of the bar code.

The Whitesides group had already developed an elegant electret based bar code system consisting of polymeric beads that tribocharge. The beads can be strung together to make sequences. The system is shown below where the blue beads acquire a positive charge and the white beads acquire a negative charge. The clear beads do not charge. The figure below is a time sequence of the folding of the structure into a sequence matched pair. Our theoretical work suggested that good self-assembly would occur when approximately 4 charged beads were strung in a succession to provide the short initial interaction. The uncharged beads were then inserted between that 4 bead charged region and the next. If the length of the clear beads is equal to the persistence length, excellent self-assembly occurs, as shown below. If the transparent spacers are shorter, more than 4 beads interact initially and the system gets trapped in false minima. If more the transparent spacers are longer, the sequences never fully assemble because the nearest neighbors of matched 4 bit sequences do not interact. A plot of successful self-assembly vs clear spacer length is shown on the bottom right below. These results confirmed our theoretical predictions and provide a basis for more general bar-code based self assembly systems.



Aksay Group – Princeton University**INHIBITION AND PROMOTION OF CORROSION****Characterization of Corrosion using Electrochemical Cells**

Corrosion dynamics and inhibition of macroscopic bulk systems have been the focus of research for centuries. A number of powerful techniques exist for measuring corrosion dynamics. Among these, electrochemical cell-based techniques stand out as the most widely used ones. Electrochemical cell measurements not only provide corrosion current, corrosion potential, and corrosion resistance data for a system under investigation but also give insight into more fundamental properties such as reaction mechanisms, thermodynamics, and properties of surface films. However, electrochemical cells that they lack spatial resolution. Because of the increasing importance of microsystems (e.g., microelectromechanical systems) and in the context of corrosion of dissimilar grains of composite materials, there is a need for spatiotemporally resolved corrosion techniques for the study of localized corrosion. Our studies on corrosion dynamics previously reported have led to the development of a novel, noninvasive method based on simple optical microscopy to spatiotemporally resolve corrosion rate measurements in specially designed model systems (Fig. 1). The spatial resolution is determined by the optical properties of the setup and the sensitivity of the method is determined by fluctuations of the illumination, noise generated by the image recording setup, and the time interval between subsequent recorded images. In our case, the sensitivity lies on the order of $50 \mu\text{A}/\text{cm}^2$ but can easily be improved.

We have demonstrated the usefulness and capabilities of our setup by measuring the dissolution dynamics of copper thin films on gold substrates, using this technique to study the effect of cetyltrimethylammonium bromide (CTAB) surfactant as a corrosion inhibitor. Surfactants, and in particular CTAB, have been used to hinder the corrosion of various metals, and many of the mechanisms by which corrosion inhibition takes place are understood. We focused on the corrosion behavior of copper in combination with a dissimilar gold cathode in a microsystem. We have shown that as the CTAB concentration increases to 0.8 mM, corrosion inhibition increases, becomes weaker as the concentration of CTAB increases above this value, showing that CTAB can act as both a corrosion inhibitor and promoter, determined by its different functions on the cathode and the anode. On gold, CTAB serves as a corrosion inhibitor by blocking the cathodic reactions. However, while it is blocking the cathodic reactions, it simultaneously promotes reactions on the copper anode. The competition

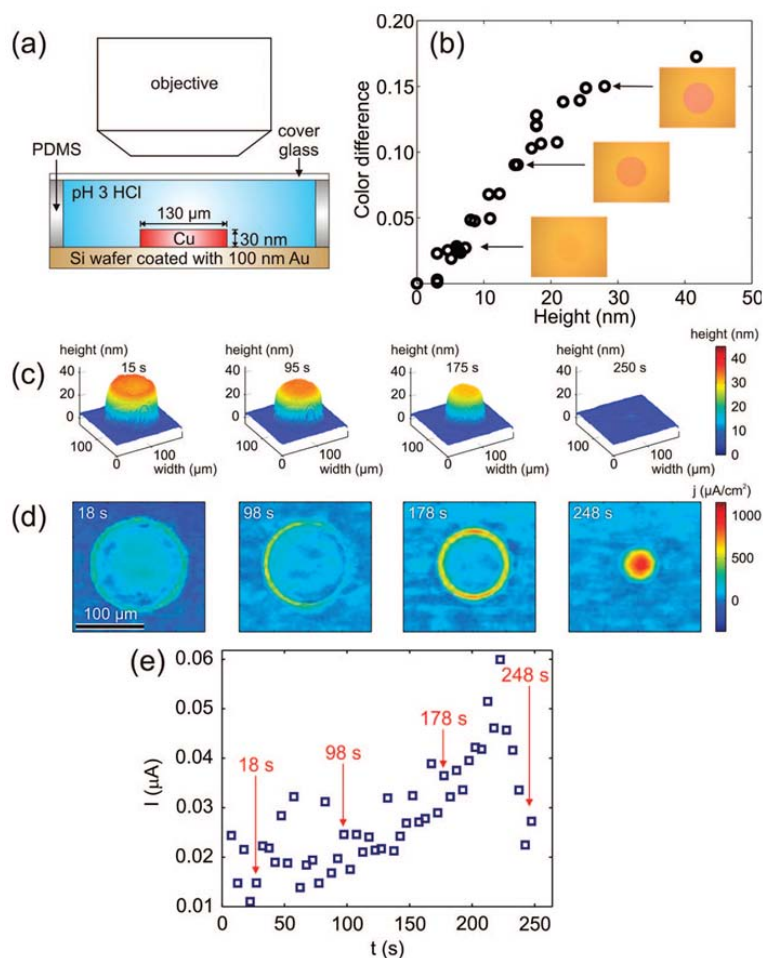


Figure 1: (a) Sketch of the experimental setup. (b) Height versus color difference calibration curve. (c) Copper disk dissolving in pH 3 HCl (aq) showing change in height and width as a function of time. (d) Estimated current density j of dissolving copper disk as a function of time. (e) Total current I of dissolving copper disk as a function of time.

between these two effects yields a minimum in the corrosion rate as the inhibitive effect of CTAB on gold saturates.

For example, topographical changes during the dissolution of a copper disk with a diameter of 130 μm and a height of about 30 nm are shown in Fig. 1c. From the color of the dissolving copper electrode, we can calculate its approximate thickness by linear interpolation between the color of the gold cathode and the initial color of the copper. By calculating the difference between thicknesses with increasing time, a dissolution rate in nanometers per second as well as a current density can be estimated (Fig. 1d), given that Cu^+ ions are the electrochemically active species on the anode. As expected for a rather low conductivity electrolyte (pH 3 HCl has a conductivity of about 200 $\mu\text{S}/\text{cm}$), the reaction is strongly localized at the rim of the copper disk. After 178 s, the reaction zone has broadened, and at $t = 248$ s, the current density is almost uniform. This change can probably be explained by a local increase of the electrolyte conductivity caused by the accumulation of reaction products and chloride ions close to the electrode surface. Thus, electrochemically active species accumulating at the dissolving copper anode must have an autocatalytic effect leading to a higher corrosion rate in the galvanic microreactor. Because of the small scale of our galvanic system, the dissolving copper disk is comparable to a corrosion pit, where the accumulation of aggressive species is known to lead to an autocatalytically induced spreading of corrosion reactions.

As a result of the heterogeneous current density, the copper electrode dissolves from the rim inward. While the outer parts of the copper island have already corroded away, the thickness at the center of the island is only slightly changed (Fig 1c, $t = 95$ s). This heterogeneity is a result of our coplanar electrode geometry and is typical for the corrosion of dissimilar metals which are immersed in low conductivity electrolyte. We can obtain an estimate for the global anodic current by the spatial integration of the current density (Fig. 1e) as a function of time. While the broadening of the reaction zone is taking place, the total current slowly increases. After 220 s, the current reaches a maximum and then decays to zero as the copper island disappears completely ($t = 250$ s). We attribute the increase in current to the aforementioned local conductivity increase. In a simplified picture, a reduced ohmic potential drop between anodic and cathodic sites increases the overpotentials on anode and cathode and thus increases the reaction rates.

As long as color variations are not affected by the formation of adlayers of reaction products on the anode, our method can be used as a powerful quantitative tool for measuring corrosion rates with high spatial and temporal resolution in microscopic model systems. The technique is not limited to copper-gold galvanic pairs, but can as well be applied to other, technically more relevant material pairs such as copper and aluminum, metal-semiconductor pairs, or metal thin films on inert surfaces. While our optical method cannot provide quantitative data about the corrosion rate in a situation where reaction products form on the dissolving anode, it provides qualitative information about the corrosion inhibition efficiency of certain corrosion inhibitors. Solely on the basis of our optical results, in an electrochemical cell configuration which is hardly accessible for classical electrochemical methods, we found both a minimum in dissolution rate as a function of inhibitor concentration and indication for the formation of reaction product layers in our system. We previously reported that we observed the same minimum in dissolution rate using zero resistance ammetry (ZRA) on bulk electrodes (Fig. 2), corroborating our results using the optical method. With ZRA measurements we explained that the minimum in dissolution rate as a function of CTAB concentration is most likely due to the catalytic action of bromide counterions on the copper surface. These measurements also show that CTAB inhibits the reaction taking place on the gold electrode. These two competing processes lead to the minimum in dissolution rate as a function of CTAB concentration.

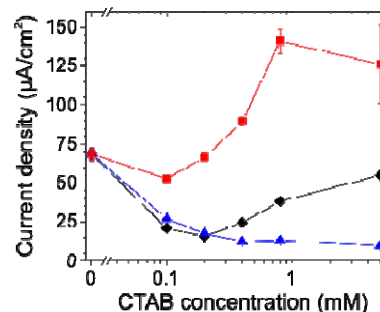


Figure 2: Current density as a function of CTAB concentration from split cell ZRA measurements. Black diamonds represent CTAB in both half cells, blue triangles represent CTAB in the gold half cell only, and red squares represent CTAB in the copper half cell only. Error bars indicate scatter in measured current values.

Control and Application of Galvanic Corrosion on the Micron Scale

We discovered two new aspects of galvanic corrosion reactions in micron scale systems. Depending on typical length scales of the corroding structures, observed reaction rates deviate from what could be intuitively expected based on the classical understanding of macroscopic corroding systems. Furthermore, spontaneous galvanic processes could be utilized for guided self-assembly of colloids. Negatively charged colloidal particles with different charge densities and specific gravities are separated and form crystalline colloidal arrays on the galvanic electrodes through a competition between electrophoretic attraction and electrokinetically induced fluid flow. This is achieved without the need of external power supplies or connections and allows for geometrically complex and versatile configurations. Our findings have important implications for fundamental corrosion studies, fabrication of pixellated structured materials, and micro-separation devices.

Two results from our experiments are shown in Fig. 3. The sample in the left image consists of copper triangles on a gold surface. During galvanic corrosion of the triangle, colloidal particles were attracted toward the anode through electrophoretic forces. They form crystalline patterns caused by microscopic flow patterns around the individual particles on the electrode surface and become permanently stuck to the surface. The sedimentation is due to reaction products depositing underneath the colloidal particles.

Similar electrokinetic effects that cause the crystallization of particles can also be utilized for particle separation purposes. This is demonstrated in the right image of Fig. 3. While strongly negatively charged polystyrene particles are attracted to the corroding copper anode (two large dark structures at the top and bottom left), slightly charges silica particles are pushed toward the interstitial regions between the anodes at the same time. This indicates that particle motion is governed by a competition between electric field induced electrophoretic particle motion and fluid flow. While electrophoretic forces attract negatively charged particles to the copper anode, the fluid flow is directed away from the anode. The velocity of colloidal particles is the sum of electrophoretic velocity and flow velocity of the surrounding electrolyte. For polystyrene particles the electrophoretic motion dominates while for silica particles the flow velocity exceeds the contribution of electrophoretic attraction.

In freely corroding galvanic systems the observed microscopic flows influence the transport of reaction educts and products. Very recent results indicate that the size- and geometry-dependent changes of the transport of chemical species in these systems have a significant influence on the dissolution rate of the copper anode. The change of flow patterns due to changes in size and geometry of the corroding structures provide control over corrosion reactions in galvanic systems.

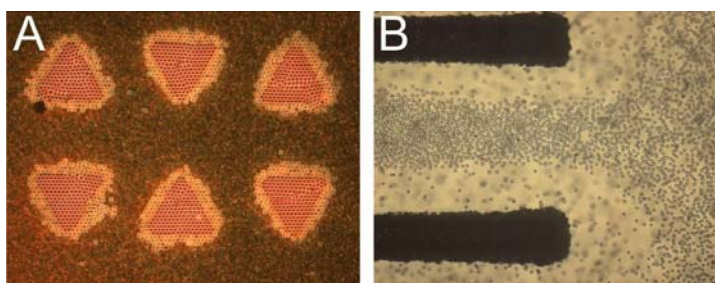


Figure 3: (A) Sedimentation of highly ordered 2.0 μm polystyrene microspheres on copper triangles. (B) Separation of particles with different zeta potential. For details, see text. Image width 430 μm .

Guiding Colloidal Crystallization in a Galvanic Micro Reactor

Colloidal crystals have been used as a tool for fundamental studies in the context of phase transitions and for the study of crystalline materials. They provide a powerful approach to fabricating sensor devices and photonic band-gap materials. A variety of techniques such as evaporation and spin coating methods or the application of external electric fields have been developed to achieve the orderly arrangement of fine particles for these purposes. Especially in photonic applications, e.g., for the fabrication of wave guides or laser cavities, both high crystallinity and patterning of the colloidal structure are necessary. Ideally, forming the colloidal crystal and patterning into the desired structure occur autonomously in one single self-organized process. However, self-assembly techniques usually produce spatially homogeneous samples, suffer from a lack of crystallinity of the colloidal aggregate, or require spatial confinement and accurate process control. To counter these issues, we developed a technique for the autonomous assembly of colloidal microspheres with spatial and orientational control to produce colloidal aggregates of high crystallinity and in complex two-dimensional patterns (Fig. 4). In our system, galvanic micro-electrodes guide the aggregation and crystallization of colloids through the interplay of electrochemical, electrokinetic and mechanical effects. Thus, galvanic corrosion is used as a “micro-tool” to fabricate a pixelated functional material. This concept can be expanded to include autonomous self-healing and adaptive materials. For example, microcracks would trigger electrochemical deposition at the damage site, thereby repairing the defects and strengthening the material.

A schematic of our apparatus is shown in Fig. 4A. A pair of electrodes (the galvanic couple) is immersed in an electrolyte suspension of colloidal particles. The galvanic reaction starts spontaneously when the acidic particle suspension contacts the copper anode and the gold cathode: The oxidation of elemental copper to soluble cuprous and cupric ions at the anode is balanced by the reduction of oxygen to hydrogen peroxide which occurs mainly on the gold cathode. As in lead-acid batteries, the ionic current flows through the electrolyte solution while the corresponding electronic current flows through the metal films. Using *in-situ* optical microscopy we observe that, while the electrochemical dissolution of copper proceeds, suspended polystyrene (PS) microspheres are attracted to the copper anodes and aggregate in a crystalline pattern. The result of an experiment using triangular copper electrodes is shown in Fig. 4B. As seen, particle monolayers deposit on each copper electrode with almost perfect crystallinity. Each triangle then forms a ‘pixel’ within a larger array (shown in the inset to Fig. 4B). In the example shown, each pixel is surrounded by a dark halo due to the deposition of reaction products on the gold cathode.

The aggregation process depends on several factors including electrode materials, cell geometry and volume, and

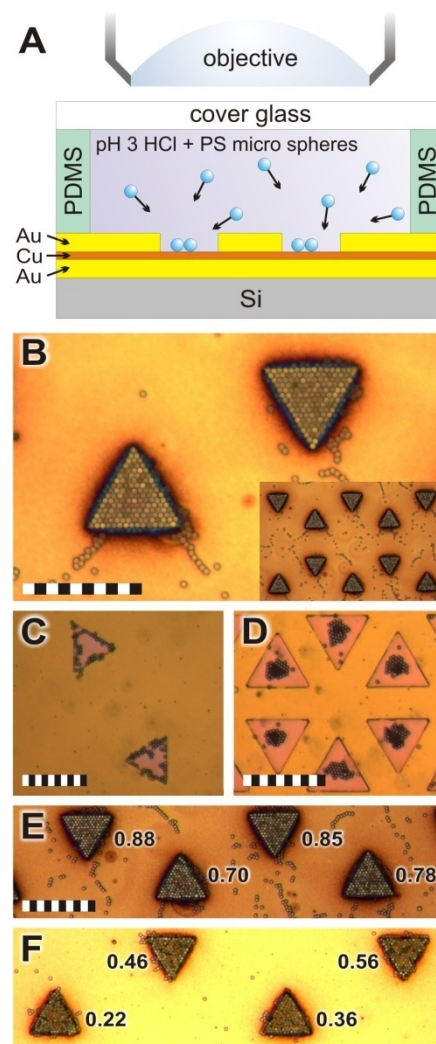


Figure 4: Guided colloidal aggregation using galvanic micro reactor arrays. Scale bars = 50 μm . (A) Schematic of the micro reactor. The patterned electrode consists of a 100 nm thick gold layer (yellow) deposited on a silicon wafer topped by a 40 nm copper film (red) and a 200 nm gold film (yellow). A pH 3 HCl (aq) solution with suspended PS microspheres (2.3 μm diameter) is used as the electrolyte. (B) 2D colloidal crystal on triangular electrodes under a suspension of 0.11 vol% PS particles, 650 μm thick PDMS spacer, and 13 min. reaction time. (C) *In situ* image of PS particles aggregating preferentially at the edges of triangular copper electrodes (40 μm triangles, 80 μm separation). (D) *In situ* image of PS particles aggregating preferentially at the centers of triangular copper electrodes (40 μm triangles, 20 μm separation). (E-F) Two different electrode configurations resulting in different crystallinity of the final aggregates.

properties of the colloidal suspension. The effect of changing electrode geometry is illustrated in Fig. 4C-D, where we show *in situ* images of PS particles aggregating on identically sized copper triangles with different inter-triangle spacing. At larger electrode separations (Fig. 4C), particles preferentially aggregate along the edges of the triangle; at small electrode separations the aggregation of particles starts at the center (Fig. 4D).

We can analyze the crystallinity of aggregated colloidal particles by calculating a quantitative order parameter ψ_6 for each pixel. In Fig. 4E and F we show two representative examples of such an analysis for two different electrode geometries. In Fig. 4E, we show a section of the result presented in Fig. 4B. In Fig. 4F, we show particles aggregated on 40 μm triangles with a separation of 80 μm under a particle concentration of 0.06 vol%. Values of the calculated order parameter ψ_6 are displayed next to the respective triangular pixel. The average ψ_6 values for the results shown in Fig. 4E and Fig. 4F are 0.78 ± 0.10 and 0.34 ± 0.17 , respectively (the analysis includes additional pixels not shown in the images). It is evident that the larger electrode spacing, combined with lower particle concentration, negatively affects pixel crystallinity and uniformity. Therefore, system parameters need to be carefully optimized in order to achieve an optimum result in terms of pixel crystallinity. In order to study the mechanisms causing particle motion in our system we performed particle tracking experiments with two different types of colloids (PS and silica) and we analyzed the associated dissolution dynamics of copper electrodes. For these experiments, we used stripe-shaped elevated copper structures ('islands') instead of trenches because doing so facilitates the necessary computer

processing of the recorded image sequences. In Fig. 5A we show the different behavior of PS and silica particles suspended in an electrochemical cell containing an array of copper stripes (only two copper stripes are shown). A separation of dyed PS particles (appearing dark in the image) and colorless silica particles (appearing bright in the image) can be observed: The copper surface is predominantly covered with PS particles while only silica particles are found on the gold cathode. We analyzed the lateral component of the motion of single PS and silica particles, i.e. their motion parallel to the electrode surface towards or away from the edges of the copper stripes (x -direction), at low volume concentrations as they moved within the electrolyte in different heights above the gold surface. Negative velocities v_x denote a transport towards the nearest copper anode and vice versa. The vertical distance y between particles and the electrode surface could roughly be estimated by focusing with a calibrated microscope stage.

To summarize the key observations, the lateral component of the velocity v_x of silica particles at a distance $y \approx 20 \mu\text{m}$ above the gold cathode is the same as v_x of PS particles, i.e., far above the gold surface, both silica and PS move towards the nearest copper electrode with $v_x \approx -1.5 \mu\text{m/s}$. On the contrary, silica particles moving in close vicinity ($y = 0 \mu\text{m}$) to the gold surface propagate away from the copper electrode with a velocity of up to about $+1.5 \mu\text{m/s}$. This cannot be understood solely based on electrophoresis. PS particles used in our experiments carry a negative surface charge and have a zeta potential of $-44 \pm 3 \text{ mV}$. Therefore, their observed lateral motion toward the high potential copper anode might be explained by electrophoretic effects. However, almost identically charged silica particles ($-39 \pm$

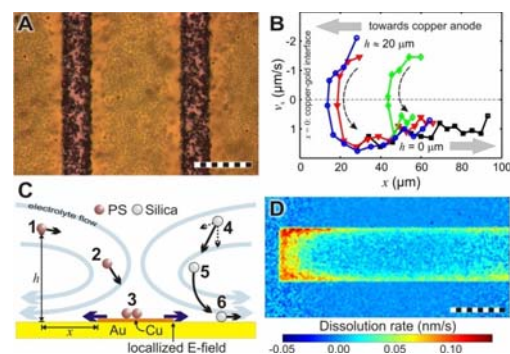


Figure 5: Particle separation and electrolyte convection. Scale bars in (A, D) are 100 μm . (A) Separation of PS (red, only on stripe-shaped copper anodes) and silica (colorless, mainly on the gold cathode) particles using a suspension of 0.22 vol% PS particles and 0.16 vol% silica particles (both $\sim 3 \mu\text{m}$ in diameter) in pH 3 HCl, 280 μm thick PDMS spacer. (B) Tracking of silica particles: Particle velocity v_x as a function of lateral distance x from the copper-gold interface. Negative velocities correspond to motion towards the copper electrode and *vice versa*. Blue circles, red triangles, and green diamonds denote positions and velocities of three different silica particles which initially are located at a vertical distance $h \approx 20 \mu\text{m}$ above the gold cathode. Black squares indicate the location and velocity of a particle already initially located directly on the gold surface at $h = 0 \mu\text{m}$. (C) Tentative schematic of particle motion and electrolyte convection close to a copper electrode. For the particle at position 1, the height h above the electrode and distance x from the copper-gold interface are indicated. (D) Heterogeneous copper dissolution rate shown for a copper stripe on gold 180 s after the reaction was initiated by addition of pH 3 HCl (aq).

4 mV) that have sunk to the gold surface are observed moving laterally away from the copper. This surprising result strongly suggests that not only electrophoresis (and in the case of silica, gravity) is responsible for the transport of colloidal particles, but that convection of the electrolyte must have a significant influence as well.

The observed behavior of the silica and PS particles can be explained by the presence of convection cells located at or near the location of every electrode interface (Fig. 5C). The driving force for these flow cells is the localized electrochemical reaction at the copper-gold electrode interfaces (Fig. 5D). In Fig. 5C we show a schematic cross section of convection cells near an electrode. At distances $y \approx 20 \mu\text{m}$ above the gold electrode surface, fluid flow (indicated by light blue arrows) is directed towards the copper electrodes. Electrophoresis and sedimentation have negligible influence on the motion of light PS particles far away from the copper anodes and they are entrained in the flow (point 1). As they approach the electrode junction (point 2), PS particles are transported into closer proximity of the copper anode since the flow is directed downwards. In close proximity to the anode, PS spheres become attracted to the copper anode probably due to the increasing contribution of electrophoresis and finally are deposited on the anode where they form crystalline patches (point 3). On the other hand, silica particles (point 4) do not closely follow the bulk fluid motion but instead sink to the gold surface since their sedimentation velocity is larger than the convective flow velocity. During their motion they leave the region where the lateral component of the flow is directed towards the copper anodes (point 5). Finally, they settle down on the gold cathode where they are entrained in the part of the electrolyte flow pattern which is directed away from the copper anode (point 6). Thus, the existence of a Faradaic current triggers the accumulation of material at a specific location. We envision adaptive materials in which local damage spontaneously generates currents that either electrophoretically or through other mechanisms cause the directed deposition of material at the damaged areas. We are continuing our investigations of this approach.

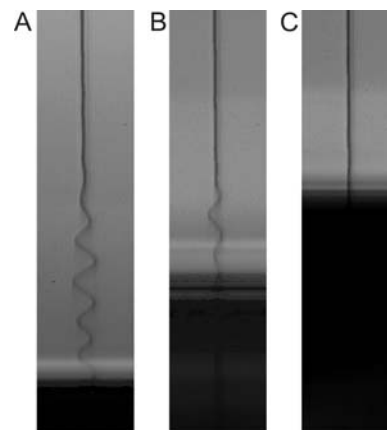


Figure 6: Glycerol jets ($4.63 \mu\text{S}/\text{cm}$) formed under $8400 \text{ V}/\text{cm}$ applied electric field, at $2.5 \text{ ml}/\text{h}$ flow rate. (A) electrode separation is 8 mm , current is $0.238 \mu\text{A}$, (B) electrode separation is 7.5 mm , current is $0.238 \mu\text{A}$, (C) electrode separation is 7.0 mm , current is $0.241 \mu\text{A}$.

ELECTROHYDRODYNAMIC PRINTING

Stabilization of EHD Jets

Electrohydrodynamic printing (EHDP) utilizes ‘stable’ electrified jets, i.e. liquid electrets, formed through a cone-jet transition at a nozzle tip to controllably deploy liquids onto moving surfaces (Fig. 6). The cone-jet transition reduces the diameter of the jet by two to three orders of magnitude compared to the diameter at the exit of the nozzle and allows for the routine production of patterns with line widths less than $10 \mu\text{m}$. Under proper conditions, line widths can be reduced to as small as 100 nm . Small feature sizes, precise positioning, and fast deposition rates are advantages of EHDP when compared to current direct printing techniques. However there are two major limitations in the use of EHDP: (i) maintaining the stability of the EHD jet during deposition and (ii) controlling the stability of the liquid lines deployed on surfaces. Jet stability is limited by the amplification of axisymmetric and non-axisymmetric deformations of the jets due to their surface charge and small diameter. We have shown that stable EHD jets can be maintained by enhancing the gas ionization around the jet either by (i) increasing the electric field through small electrode separations or (ii) changing the composition of the atmosphere in the chamber containing the jet. The liquid line stability is affected by the capillary breakup of the patterned liquid lines on surfaces. This can be adjusted by controlling the rate of evaporation of the solvent and/or by changing the breakup time, a function of the wetting characteristics of the liquid on the substrate.

For high precision deposition, it is important to minimize the deflections of the jet at the bottom electrode. Assuming that any initial disturbance (ξ_0) is allowed to grow during the time of flight, it is

possible to estimate the maximum deflection of the jet by using the instability growth rates (ω) from $\xi = \xi_0 \exp(\omega l / v)$, where l is the length and v is the average velocity of the jet. Fig. 7A shows the calculated maximum deflection of jets formed between closely separated electrodes and those formed between distant electrodes. Each point in the lower curve indicates the maximum deflection of a jet formed between the separations given by the x -axis, at the point it reaches the bottom electrode. Points in the upper curve refer to the maximum deflection of a jet formed between electrodes separated by 20 mm, at the position given by the x -axis. The information in Fig. 7A shows that the deflections of the short jets are close to zero whereas the deflections of long jets can be as large as tens of micrometers. In order to obtain this plot, the amplitude is estimated to be 2.5×10^{-10} m by assuming that the source of the initial disturbances is due to the thermal energy of the gas molecules. Although this curve is useful in terms of indicating the behavior of the jets, accurate quantitative estimations require the upper limit for the initial disturbance amplitude to be known in a given environment. However, for the purposes of deposition and printing applications, we can measure the maximum deflection of the jets directly from experimental images taken of liquid jets of composition relevant for proposed applications.

For example, in Fig. 7B we show the maximum centerline deflection of polyethylene oxide (PEO) jets at the same point along their length. The curve shown in Fig. 7B looks almost linear, whereas theoretically centerline deflection is expected to increase exponentially as shown in Fig. 7A. This apparent discrepancy is because the field of view of our optical system allows only part of a single wave to be observed in PEO jets. Figs. 7C and D show that distributions of deflections are symmetric around zero and resemble normal distribution. This supports the hypothesis that the disturbances are indeed random. Fig. 7B also demonstrates that the difference between the maximum deflections of the short and long jets can be as large as 100 μm . Therefore, by decreasing the electrode separation a major improvement in the precision of printing can be achieved.

Colloidal Clusters through EHDP

In this part of our research, we focused on EHDP of suspensions with polymeric solutions of polar fluids on a hydrophobic substrate. Due to non-wetting conditions, the lines break up and yield arrays of colloidal clusters. Arrays of well defined structures of colloidal clusters are not only of technological interest due to potential applications such as superhydrophobic surfaces, optoelectronic devices, seeds for building larger three dimensional structures, and lithographical masks, but also of scientific interest as analogs of atomic clusters.

Using a motion system that consists of a rotary table and a linear motor, we EHD printed on hexadecanethiol coated surfaces with (i) a PEO solution and (ii) a suspension of polystyrene particles (3.1 μm in diameter at 0.77 % by volume) in a PEO

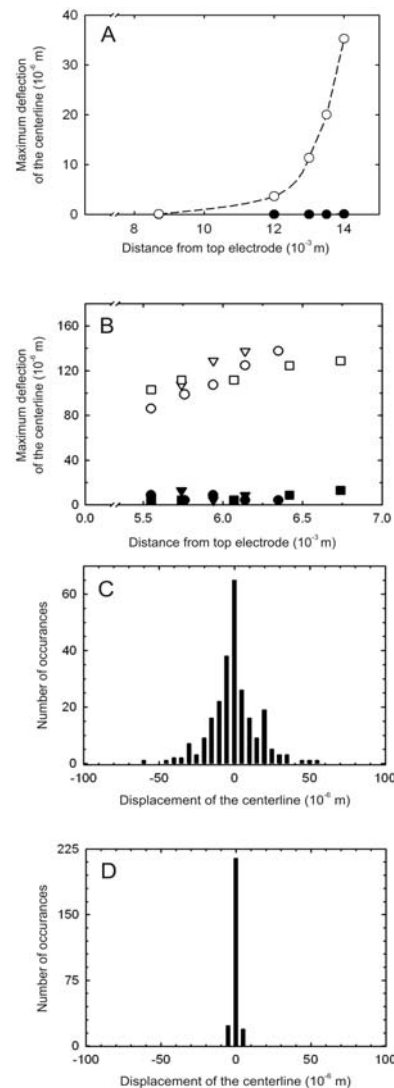


Figure 7: (A-B) Comparison of centerline deflection of at the deployment point on a bottom electrode produced with small electrode separations (filled symbols) vs. the centerline deflection of a jet formed between large electrode separations (open symbols) at the equivalent position with respect to the nozzle. (A) Calculated from instability growth rates for glycerol jet under 12 ml/h flow rate and 9430 V/cm electric field. Large electrode separation is 20 mm. (B) From experimentally determined images of a PEO solution jet under 1 ml/h flow rate and 4119 V/cm electric field. Large electrode separation is 25.1 mm. (C-D) Distributions of deflection centerline for PEO solution jets formed between electrodes separated by (C) 25.1 mm and (D) 5.7 mm at 5.7 mm from the top electrode.

solution (Fig. 8A and B, respectively). Both patterns were produced under the same printing conditions. Although the jet was deployed on the surface as a continuous ‘line,’ the deployed liquid filament was unstable and broke up into drops since the contact angle^{xiii} was greater than 90° and the contact lines were not pinned. This break up is due to a 2D version of Rayleigh instability caused by capillarity. When the instability sets in, the lines bulge in some parts and thin down in between the bulges. Main drops form from the bulges, whereas the satellite drops form as result of detachment of the thin section of the liquid from the bulges. The diameters of the main islands shown in Figures 8A and B are $7.5 \pm 0.6 \mu\text{m}$ and $7.9 \pm 0.7 \mu\text{m}$, respectively. The islands align in rows that make less than 1° angle with each other, whereas particles deviate $\pm 3.5 \mu\text{m}$ from a straight line since colloidal particles are located randomly within the polymer residues (Fig. 8C). The average separation between the main islands in each row in Figures 6A and B is $56.8 \pm 7.5 \mu\text{m}$ and $76.2 \pm 16.4 \mu\text{m}$, and the distance between the rows is $95.2 \pm 6.6 \mu\text{m}$ and $141 \pm 7.0 \mu\text{m}$, respectively.

There are three main geometrical features that define the arrays: (i) the size of individual islands produced by the drops, (ii) the separation between the islands within a row, and (iii) the distance between the rows of the islands. We demonstrated that all of these parameters can be controlled and estimated. The wavelength of the fastest growing disturbance defines the center-to-center separation between the main drops. We used the linear axisymmetric stability theory for a viscous jet to estimate the expected dominant wavelength due to the lack of a theory for capillary instability of viscous liquid filaments on substrates and found that the length of the fastest growing wave ($\sim 60.7 \mu\text{m}$) is fairly close to the experimentally observed island to island separation of $56.8 \pm 7.5 \mu\text{m}$ (Fig. 8A) for the PEO solution without the particles. Hence, despite the existence of the substrate, the theory for a jet break up provides a good guideline for controlling the center-to-center separation between the individual islands. The length of the fastest growing wave, λ , and the cross sectional area of the liquid at the time of the break up defines the initial volume of an island as $Q\lambda/v$. The maximum size of the islands prior to the evaporation of the solvent can be found taking the shape of a spherical cap: $R \sim (3Q\lambda/2v\pi)^{1/3}$. The final size of the islands is determined depending on at what stage of the evaporation the contact line gets pinned, how much of the liquid gets consumed by the satellite drops and how many particles are in an island.

A straight EHD jet with negligible bending enables the printing of parallel rows. Separation between the rows, d , is controlled by the angular velocity of the rotary table and the radial velocity of the linear motion. It is given by $d = V_r/V_\theta$, where V_r and V_θ are the radial and angular velocities respectively. Given this relationship, the expected values of d for the patterns shown in Figures 6A and B are 100 and $150 \mu\text{m}$. Experimental measurements agree well with the expectations and the difference is possibly due to the limited accuracy of the equipment and slight bending of the jet.

Figure 9 demonstrates arrays produced with a concentrated (15 % of $5.7 \mu\text{m}$ polystyrene) suspension. After the capillary break up, particles self assemble in a ‘berry-like’ three dimensional structure (inset of Figure 9). The self

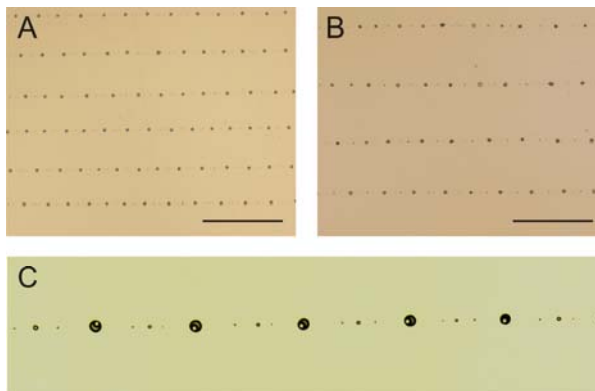


Figure 8: Optical microscope images of patterns on a hexadecanathiol coated surface produced by EHDP of (A) a PEO solution in ethanol and water, (B) a suspension of polystyrene particles in the PEO solution, (C) a single particle array of $3.1 \mu\text{m}$ particles produced by EHDP. The scale bars designate $200 \mu\text{m}$ in both A and B.

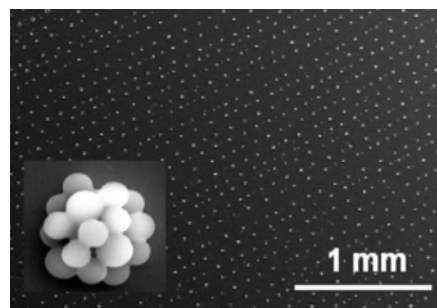


Figure 9: A scanning electron microscope image of arrays of self-assembled $5.7 \mu\text{m}$ polystyrene particles after EHDP of a suspension on a hydrophobic substrate. The inset shows a higher magnification of one of the clusters which appear as white points in the lower magnification image.

assembly is controlled by the capillary forces on the particles. Other effects such as gravitational force and the evaporation driven flow are negligible: during the time of evaporation, particles are expected to move less than a micrometer due to gravity, and the observation of tracer particles in an evaporating sessile drop on a substrate prepared the same way revealed no preferential motion of particles towards contact lines. Figure 10 shows the most frequently observed structures from EHDP of a suspension containing 6 % particles ($5.7\ \mu\text{m}$) by volume on a hexadecanethiol coated gold surface. A minimum of 150 clusters was investigated for each number of particles per cluster. The clusters shown in Figure 10 for 2, 3, 4, 5, and 6 number of particles occurred 100, 86, 48, 40, and 35 % of the time, respectively.

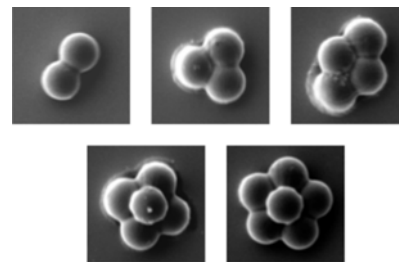


Figure 10: The most common structures of colloidal clusters, composed of different number of $5.7\ \mu\text{m}$ diameter polystyrene particles, produced on a 1-hexadecanethiol coated gold surface from EHDP of the colloidal suspension.

We found that the structure of the clusters formed on the substrate is different than what has been reported previously as a result of evaporation from a fully spherical drop in the absence of a substrate (Fig. 10) with the exception of the two and three particle cases. The existence of the substrate affects the packing of the particles in two ways: (i) by introducing capillary interactions between particles and the substrate, and (ii) by limiting the height of the drop and the available area for packing of particles at the interface. Capillary interactions between particles and the substrate differ from capillary interactions between two particles not only in magnitude but also in direction. Capillary interactions between the particles and the substrate can be either attractive or repulsive depending on the contact angle of the particle and the substrate with the liquid; whereas the capillary interactions between chemically identical particles are always attractive type. Therefore, in the presence of a substrate, forces experienced by the particles vary depending on their location on the drop, which breaks the spherical symmetry.

COLLOIDAL ARRAYS IN ELASTOMERS

Dielectric Strength Measurements of Field-Type Elastomers

Dimensional strain of over 100 % has been demonstrated on elastomeric actuators upon high voltage actuation. The underlying principle is that a compressive Maxwell electrical stress arises when a dielectric material is subjected to an intense external electric field, and this stress acts to cause deformation of the material. Here, we employed two spherical electrodes in dielectric breakdown measurements to circumvent the pre-mature failure problem encountered in previous studies where plate-like electrodes were used. A laser technique was also invented to track the thickness change of the actuator for accurate quantification of electric field strength during the breakdown test. Since these actuators are prone to electrical breakdown that limits their peak performances, our accurate measurements of dielectric strength are crucial for reliable actuator designs and systematic material improvement.

Figure 11 illustrates the schematic of our experimental setup. A given acrylic film (VHB4905, 3M) with initial thickness of 0.5 mm was pre-stretched in the lateral directions, placed on a rigid frame and sandwiched between two stainless steel spherical electrodes. As the applied voltage drop across the two electrodes was increased linearly from 0 V until electrical breakdown occurred, the acrylic film was compressed by the electrostatic force from the two spheres. The thickness reduction of the film led to vertical displacement of the upper sphere and the attached lever. The tracking of the lever position with a laser enabled quantification of the film thickness change. The setup was synchronized to

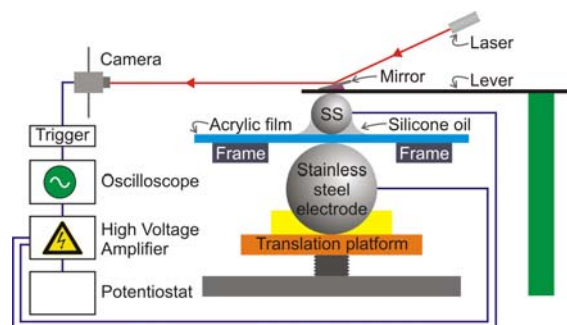


Figure 11: Schematic depiction of the apparatus for measurement of thickness change during application of high voltages.

allow accurate determination of the moment when breakdown took place.

Experiments were performed on 24 samples with 100 % × 100 % pre-stretch and 21 samples with 200 % × 200 % pre-stretch. Figure 12 presents results in terms of normalized thickness versus field strength. Here, we define field strength as the applied voltage divided by the instantaneous thickness of the acrylic film being deformed. It is obvious that electromechanical response profiles of the two batches of trials are consistent. The average dielectric strength for samples with 100 % × 100 % pre-stretch was found to be 299 MV/m, with a standard deviation of 96 MV/m. Whereas the average value for samples with 200 % × 200 % pre-stretch is 399 MV/m, with a standard deviation of 94 MV/m. The reported values in literature for samples with 100 % × 100 % and 200 % × 200 % pre-stretch are 60 MV/m and 100 MV/m, respectively. Such severe underestimation by previous investigators was due to premature breakdown associated with the presence of concentrated electric field distribution at sharp corners of plate-like electrodes. The relative difference in the average dielectric strength for samples with 100 % × 100 % pre-stretch and 200 % × 200 % pre-stretch is small in comparison to what was published. The trend of modest increase in breakdown strength with pre-straining as observed in our study may be explained by the well known probabilistic correlation between the probability of failure and the sample thickness.

We have modeled our setup that consists of the acrylic film, the high voltage source, and the two spherical electrodes as a thermodynamic system. The free energy of the system with respect to the state of zero applied voltage is given by Eq. 1:

$$G = \frac{1}{8\pi\epsilon Rf(H/R, \lambda)} Q^2 + \mu H^3 g(H/R, \lambda_o, \lambda) - F(\lambda - \lambda_o)H - VQ. \quad (1)$$

It consists of the electrostatic energy of the capacitor-like setup, the elastic energy of the strained acrylic film, the mechanical energy of the cantilever, and the energy of the voltage source. Here, R , H , λ_o , λ , ϵ , Q , V , μ , f , g , and F are the radius of the upper spherical electrode, the thickness of the acrylic film in the unstressed state, the fraction of the original film thickness after the pre-stretching step, the fraction of the original film thickness during the actuation process, the dielectric constant of the acrylic film, the electric charge on the upper sphere, the voltage drop across the two electrodes, the shear modulus of the acrylic film, a function for determination of the electrostatic energy, a function that characterizes the elastic energy, and the force exerted on the upper sphere by the cantilever, respectively. Figure 16 shows comparisons between the model and selected sets of data in terms of dimensionless voltage and thickness. The theoretical model was found to be in excellent agreement with the electromechanical response data.

Structural Color

In the past decade, considerable attention has been given to the study of field-type elastomeric actuators which exhibit strains of over 100% upon application of electrical fields. Their large actuation amplitudes far exceed the capabilities of traditional piezoelectric materials or electrostrictive and ionic-based shape-changing polymers. A field-type elastomeric actuator requires mechanically compliant electrodes which adhere to its surface and do not impose mechanical impedance upon actuation. Conventionally, carbon grease is chosen as an electrode material because it has a high electric conductivity and can follow the motion of the actuator without interfering mechanically. Its use has been successfully demonstrated in the early stage of actuator development as well as in recent studies, e.g., on the application of field-type actuators in display technology.

However, using carbon grease electrodes in an application has severe disadvantages. It is prone to spreading during actuation, cannot serve as a top surface of the device, its surface cannot be patterned and

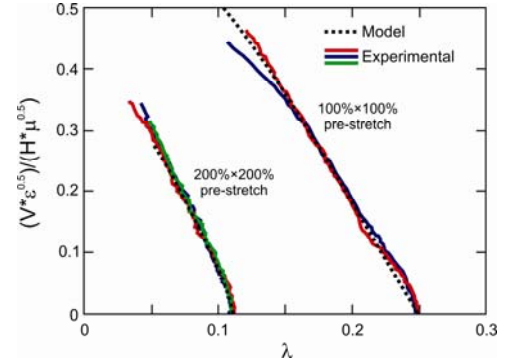


Figure 12: Comparisons between the theoretical model and the selected sets of experimental data in terms of a dimensionless voltage and a dimensional thickness.

DESIGN AND PROCESSING OF ELECTRET STRUCTURES

it fails to transfer shear stress to adjacent material layers since it is a viscous liquid. Therefore, extra steps such as building a physical confinement for the electrode are necessary for practical applications. We have developed an elastomeric composite consisting of polydimethylsiloxane (PDMS) filled with functionalized graphene sheets (FGS) and use it as an electrode material for field-type actuators (Fig. 13). It exhibits good electrical conductivity and is compliant if applied in a sufficiently thin layer. In contrast to carbon grease, its elastic nature enables retention of dimensional shape after repeated actuation. It can be directly surface-patterned and offers the option of using the electrode for shear stress transfer between the actuator and other design elements. Unlike in the case of polymers with high contents of conventional carbon filler such as carbon black, the low concentration threshold for electrical percolation (0.2 wt% filler loading) of our material renders it highly elastic and remains similar to the properties of pristine PDMS. This paves the way to using soft-lithography techniques for creating miniaturized electrode geometries. Further, the surface of the FGS-based compliant electrode is smooth and can be easily patterned during the curing process of the polymer.

Actuations of three dimensional photonic elastic film, produced by convective self-assembly of 520 nm silica colloidal particles and subsequent infiltration with PDMS, were carried out as a demonstration of possible application to structural color display. Fig. 13A shows an SEM image of a crystalline nanoparticle array infiltrated with PDMS. A layer of FGS-PDMS (0.5 wt % loading) composite was spin-coated on the elastic photonic film to serve as an electrode. The elastic photonic film (50 μm thick) was then adhered to an acrylic film (with initial thickness of 1 mm and pre-stretched by 300 % \times 300 %) driven by Maxwell stress. Carbon grease was smeared onto the bottom side of the acrylic film and functioned as mechanically compliant electrode. As oscillatory voltage drop with amplitude of 5 kV and frequency of 0.5 Hz was applied across the composite electrode and the carbon grease electrode, the acrylic film was stretched laterally by electrostatic force. This deformation led to the lateral expansion of the elastic photonic film adhered to the acrylic film, causing a change in the spacing between the packed colloidal spheres and thus an alteration of the observed structural color. Fig. 13B-D present the change of color realized through application of voltage drop. The observed wavelength of the reflected color increases, blue towards red. This implies that the spacing of the planes from which light diffracts expands as the elastic photonic film was deformed. Note that color continuous changed as the applied voltage was increased and that the initial color at zero voltage was determined by the angle which the camera makes with the sample surface. With the electromechanical induced strain on the order of 15%, an initially blue surface can be tuned to green, while an initially green surface can be tuned to deep orange. In this sample, the applied voltage was kept at or below 5 kV to ensure electrical failure did not occur during actuation. The large color tuning range presents a potential for development of this structural color element into practical display technology.

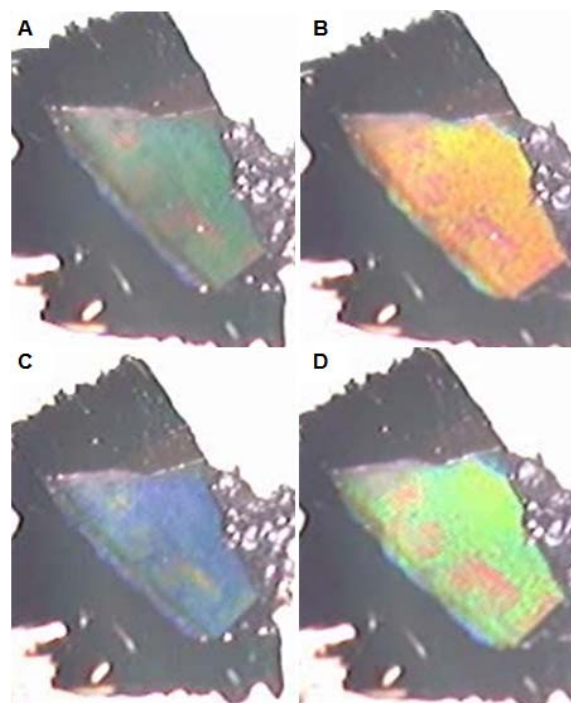


Figure 13: Color changes in a composite made from a nanoparticle crystalline array in PDMS on a compliant FGS/PDMS electrode. (A) Composite in quiescent state. (B, C, D) Color changes induced by changes in voltage.

SURFACTANTS ON SURFACES

Orientational Order

Surfactant aggregates exhibit strong, lattice-induced orientational order on a number of atomically smooth, crystalline substrates. There have been several earlier attempts to rationalize this

order either originating from a crystalline anisotropy in the van der Waals interactions or as induced orientational order from topographic steps. The latter view is not in agreement with a substantial amount of the reported experimental evidence: the great majority of surfactant micelles on highly oriented pyrolytic graphite (HOPG) surfaces run perpendicularly with respect to the lattice symmetry axes, whereas the steps on cleaved HOPG are often unrelated to these axes. Liquid-cell scanning tunneling microscopy studies of surfactants on Au(111) surfaces at elevated electrical potentials revealed monolayers of surfactant molecules epitactically grown on Au(111) indicating that the orientation of surfactant micelles is templated by a flat surfactant layer. However, there is no direct evidence that the first layer of surfactant molecules in surfactant micelles exhibits crystalline order.

In order to understand the conditions leading to this transition from the lattice-induced orientational order to topography induced orientational order, we use single-atomic steps as model topographic features and demonstrate that the atomic steps are indeed capable of orienting surfactant micelles. Our results reveal a competition between lattice-induced and topography-induced orientational order. Based on these micellar resolution images we show that the relative strength of these two mechanisms depends on the surfactant/substrate combination.

The result of liquid-cell AFM at the interface of a graphite(0001) surface and a 10 mM C₁₆TAC solution is shown in Figure 14. Figure 14a shows an image obtained with a high vertical force, such that the tip made direct contact with the graphite substrate. This is proven by the high-resolution scan revealing the graphite lattice (top inset, lattice symmetry axes $\alpha_1/\alpha_2/\alpha_3$ highlighted by pink/mint green/violet arrows, respectively). The top half of Figure 14a is virtually defect free, whereas the bottom half shows several single-atomic steps on the surface. The topography section across three of those steps following the light blue, dashed line shows that the observed step height is in agreement with the expected 0.34 nm *d*0002 spacing of graphite. The direction of this cross-section was chosen strictly parallel to the fast scanning direction in order to minimize inaccuracy due to drift and piezo creep. Figure 14b was taken at low force and visualizes the C₁₆TAC surface micelles, which are known to be of hemicylindrical morphology. In agreement with previous reports, on the majority of the surface, the micelles are oriented in directions $\beta_1/\beta_2/\beta_3$, perpendicularly with respect to the $\alpha_1/\alpha_2/\alpha_3$ lattice directions. However, we observe that not all micelles are oriented according to this previously reported rule. In the vicinity of the topographic steps on the graphite substrate, some micelles are oriented parallel to these steps at an angle of about 15° with respect to the usually preferred β_3 direction. Using topography cross-sections we determined that these micelles had the same height as micelles further away from the step. A typical topography section across several of the micelle-covered HOPG steps following the light blue, dashed line is shown in Figure 14c, top. The obtained profile is very similar to the one shown in Figure 14a, except the topography is now periodically modulated by the micelle population with an amplitude of about 0.2 nm. This means that within the precision of the measurement (~0.1 nm) all surface micelles have identical heights. It is thus safe to assume that the micelles in the vicinity of topographic steps of the substrate are also hemicylindrical. If they were full cylindrical micelles, they would have been easily detected, as they should be ~2 nm higher than hemicylinders.

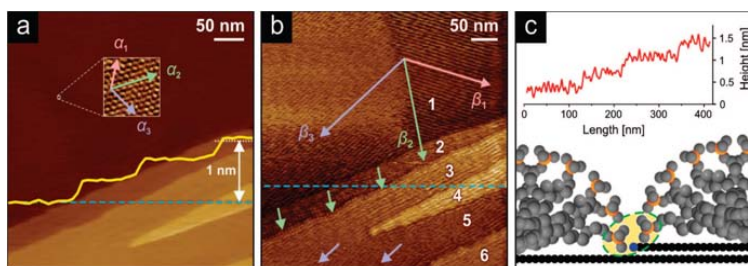


Figure 14. (a) High-force AFM topography image of graphite in 10 mM C₁₆TAC, showing the substrate. The yellow topography cross-section follows the light blue, dashed line and features single-atomic steps. The high-resolution inset shows the graphite lattice orientation with symmetry axes $\alpha_1/\alpha_2/\alpha_3$. (b) Imaging the same system at low force reveals the surface micelles with preferred orientations $\beta_1/\beta_2/\beta_3$. White numbers designate terrace areas, separated by ledges. (c) Top: topography cross-section following the light blue, dashed line in (b), showing the topography modulation on the terraces due to micelle coverage. Bottom: schematic of two hemicylindrical micelles at a topographic step (gray and black atoms: carbon, orange atoms: nitrogen). The highlighted area is the interaction zone between a step and the adjacent head groups.

Similar to $C_{16}TAC$, SDS exhibits preferred orientation of the adsorbed micelles on atomically smooth Au (111). The low force AFM topography image presented in Figure 15a shows a flame-annealed gold surface in contact with a 10 mM aqueous solution of SDS. The majority of the micelles are oriented in one of the three preferred directions (parallel to the yellow arrows). The exceptions are highlighted by light blue ellipses. In all these highlighted examples, the micelles follow the boundaries between areas of different substrate heights (represented in the image by different brightness/color). Although not directly visible in Figure 15a, we conjecture that atomic steps in the substrate account for these height differences, and that the expected step directions coincide with the observed orientations of the micelles. We thus conclude that SDS micelles are also subject to orientation at topographic steps on Au(111), overriding the lattice-induced orientation. Figure 15b shows the micelles adsorbed from a 10 mM SDS solution on the unannealed, rough gold surface. It features the typical “rolling hill” morphology with a peak-to-peak topography of ~ 10 nm as shown by the topography profile (in yellow) along the light blue, dashed line of the inset. The substrate surface is purely Au(111) as determined by XRD analysis. Nevertheless, only a small minority of the surface micelles highlighted by orange arrows exhibits the linear, parallel morphology characteristic of micelles adsorbed on atomically flat Au(111). The topography profile of Figure 15b shows that micelles are linear and parallel only in flat areas where no or a few topographic steps are to be expected. The higher-magnification topography image presented in Figure 15c shows more clearly not only the flat areas populated by straight micelles (highlighted by yellow circles), but also the areas with significant topography, featuring micelle population of a more disordered morphology (highlighted by light blue circles). Analyzing many AFM images similar to Figure 15b and c, we found 19 grains showing straight, parallel micelles of two or three different orientations on a single grain, as highlighted in Figure 15c by the arrows in the large yellow circle. In all cases these directions had relative angles of $120^\circ \pm 4^\circ$. From this, we conclude that on rough surfaces the orientation of straight micelles is also lattice-controlled. On even rougher samples there are no more apparent areas that exhibit straight and parallel micelles, as shown in the AFM deflection image of Figure 15d. Although these micellar structures first seem very disordered, a closer analysis reveals that the micelles are entwining around the gold grains, similar to the contour lines on a relief map (highlighted by orange arrows in Figure 15b and d). Since the atomic steps on a Au(111) surface represent lines of constant height, this observation is in line with our previously discussed finding that SDS micelles tend to align with topographic steps. Thus, we are able to rationalize the structural appearance of elongated SDS micelles on topography-rich gold surfaces: in areas with topographic changes, the micelle orientation is determined by surface steps; in flat areas orientational registry with the substrate lattice is enforced.

We have thus shown that the spatial conformation of micellar surfactant aggregates depends on not only the crystal symmetry but also on the topographic morphology of the substrate. On many defect free, crystalline surfaces, the surfactant micelles are oriented perpendicular with

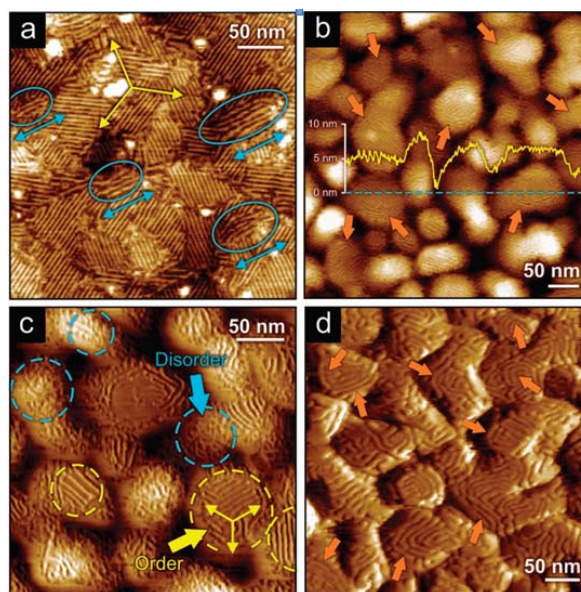


Figure 15: AFM images of gold surfaces in contact with a 10 mM SDS solution. (a) On large, flat areas the micelles are oriented in one of three preferred orientations (highlighted by yellow arrows). Only at topographic steps micelles exhibit orientations in different directions (highlighted by light blue arrows and ellipses). (b) On rougher surfaces only the flat areas show orientational order. Inset: substrate roughness visualized in cross-section following the dashed, light blue line. (c) Close-up of the sample shown in (b), revealing ordered (yellow) and disordered (light blue) areas. (d) On rougher substrates with smaller grain sizes, the micelles do not show preferred orientations. The orange arrows denote areas in which the micelles entwine around the grains (panels (b), (d)).

DESIGN AND PROCESSING OF ELECTRET STRUCTURES

respect to the surface lattice symmetry axes. When topographic surface steps are present, oriented adsorption along such steps is preferred and overrides the lattice-induced orientation. For the case of the C_{16} TAB micelles observed on Au(111), topography-induced orientation dominates the organization of all micelles. In contrast, the organization of C_{16} TAC micelles on Au(111) seems to be strongly dominated by lattice-induced orientation. For C_{16} TAC on graphite and SDS on Au(111), we observe a competition between the two mechanisms. As demonstrated for the system SDS/Au(111), the observed micellar morphology depends strongly on the topography of the substrate: on an atomically flat substrate, perfect orientation perpendicular to the lattice symmetry axes can be observed; on a sample with feature-rich topography, the lattice-induced orientation can be completely overruled by topography-induced orientation.

The Statics and Dynamics of Surfactant Surface Aggregates

With liquid cell AFM, spatial resolutions in the sub-nanometer regime and temporal resolutions on the level of seconds can be achieved. One can study the effect of many parameters of the system such as surfactant concentration, ionic strength, etc., and changes of the aggregate structures can be monitored as a function of time. Using simple model surfactants such as sodium dodecyl sulfate (SDS) or cetyltrimethylammonium chloride (CTAC), we demonstrate the influence of the structure of the solid surface on the shape of the surfactant aggregates. Crystalline surfaces often have anisotropic dielectric properties, which causes anisotropic van der Waals interactions. We have been able to show that this anisotropy is strong enough to induce orientation of cylindrical surfactant aggregates with respect to the lattice of the surface lattice.

In addition to imaging of surfactant aggregates on atomically flat substrates, we were the first to image these structures on rough surfaces. An example is shown in Figure 16, where the results obtained with an un-annealed gold surface are displayed. In contrast to crystalline surfaces, the aggregates form meandering hemi-cylinders that are arranged on the gold grains in a peculiar way. To understand the mechanism for this roughness-dependent aggregation, we tried to achieve a surface structure that is between the rough topography and the atomically flat state studied before. We therefore exposed the rough gold surfaces to the annealing hydrogen flame for a very short time at a bigger distance. The result is a gold surface on which atomic terraces are much more clearly visible as compared to the un-annealed samples. The topography, however, is still considerably rough, as the surface still shows grains. In contrast to the rough gold, the grains are not very round but show corners and edges. Their heights and diameters, however, are very close to the un-annealed gold surface. Nevertheless, the surfactant aggregates on these surfaces are perfectly linear without any curls. It is still unclear where the transition between the two different regimes of organization happens and what are the mechanisms.

These two examples the dynamic behavior of the aggregates lead us to the conclusion that these orientation processes take place on the molecular level, as they cannot be performed without decomposing the surface micelles.

Self-Healing of Surfactant Surface Micelles

Since typical AFM acquisition times are on the order of minutes, AFM studies treat surfactant aggregates as seemingly static, neglecting their dynamic behavior at different timescales. While the lateral diffusion rates of individual surfactants within flat surfactant layers are known, the actual aggregation of molecules into micelles and their organization into micellar crystals are potentially much slower. Similarly, in bulk surfactant solutions the exchange time of surfactant monomers between micellar aggregates and the solvent – $\tau_{1,bulk}$, micro- to milliseconds – is much faster than the formation time of an entire micelle from individual molecules and the corresponding disintegration time – $\tau_{2,bulk}$, milliseconds. Using AFM force-displacement curves at different approach frequencies, Clark and Ducker suggested that the reorganization of surfactants on a silica surface may occur within times as short as 20 ms. However, since the force-displacement method does not provide images, it is impossible to know if the micellar film was punctured or only compressed. Thus, their results cannot be used to draw definite conclusions on how fast surfactants self-assemble into micellar arrays on surfaces. With our technique, the AFM tip demonstrably pierces the surfactant adlayer, thereby imaging the lattice of the underlying substrate (Fig. 17). Using the same tip, simultaneously we image the micellar structure of the adlayer on the substrate and thus are able to immediately monitor the adlayer's response to the tip-induced defect.

In previous AFM imaging studies of surfactant surface aggregates, very low force set points were used to keep the tip above the very weakly bound aggregate layer through repulsive forces in the electric double-layer. Fig. 17a shows the crystalline array of hemi-cylindrical surface micelles that exists under these conditions at the interface of highly oriented pyrolytic graphite (HOPG) and a 10 mM solution of sodium dodecyl sulfate (SDS). If the force is then increased by just a few hundred pN, the probe overwhelms the repulsive force, pierces the surfactant layer and makes contact with the substrate. In this case, the substrate rather than the adsorbate is imaged.

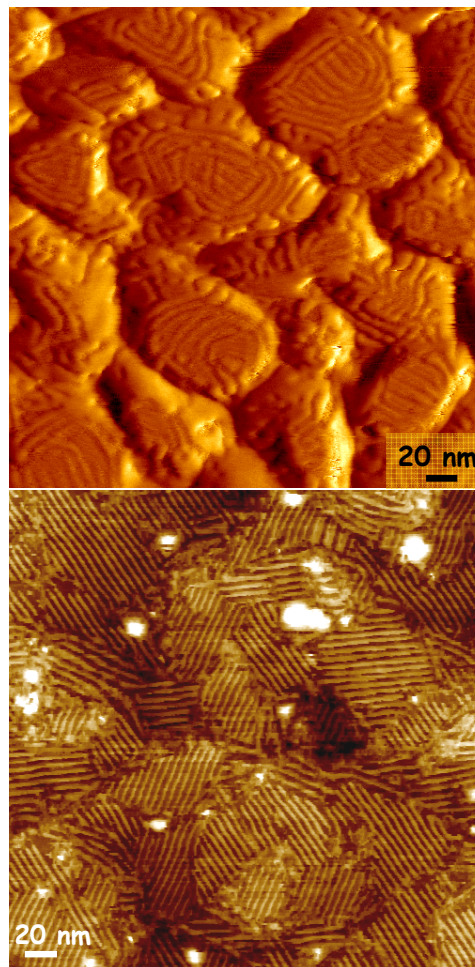


Figure 16: On an un-annealed, rough gold surface, the surfactants are not strictly linear any more, but form curled hemi-cylinders. If the surface is only briefly, it remains rough, with similar grain dimensions than in the un-annealed case, but with much more clearly visible atomic steps (AFM image, not shown). Surfactant aggregates on such surfaces are again oriented with respect to the lattice orientation.

Our new imaging technique purposely operates in this high-force regime. In addition to acquiring the deflection and topography signals as in previous work, we also monitor the cantilever torsion which represents the friction between tip and sample. As expected, this friction signal reveals the honeycomb lattice of the graphite substrate, without any apparent signal from the surfactant aggregates, shown in Fig. 17b. When larger areas are scanned under otherwise identical parameters, the friction images not only show the lattice, but – surprisingly – the signature of the micellar aggregates simultaneously, visible in Fig. 17c in the shape of diagonal stripes. At the reduced magnification necessary to reveal this micellar signal, the much smaller graphite lattice is very hard to recognize in what appears to be background “noise”. It is, however, easily revealed by the Fourier transform of Fig. 17c, displayed as an inset to Fig. 17c, conveniently demonstrating the simultaneous imaging of micelles and lattice at two significantly different length scales: the stripes in Fig. 17c, produced by the hemi-cylindrical micelles, translate into two dots close to the center of the transform; the honeycomb lattice of graphite is represented by the hexagonal pattern at much higher spatial frequencies. The blue and green lines superimposed on the inset image highlight the orientation of the substrate lattice and the micellar array, respectively, confirming that the surfactant structures are – within the precision of our technique – oriented perpendicular with a symmetry axis of the HOPG lattice, as expected. Application of a band-pass filter to Fig. 5c increases the visibility of the stripes (Fig. 17d) and allows us to determine the stripe periodicity as 5.3 ± 0.5 nm, in excellent agreement with the results of the traditional low-force imaging mode (Fig. 17a).

We explain the imaging behavior by referring to the simplified schematic in Fig. 18. The observation that all our high-force images show the substrate lattice with its 140 pm bond length proves that the AFM tip is in contact with the substrate in the region denoted by “1”, giving rise to the atomic-scale friction modulations. We estimate that the surfactant adlayer is completely displaced in a circular area of at least 9 nm in diameter. As the tip is moved towards the right, it contacts the surfactant layer in the areas denoted by “2” and ultimately strips these periodically adsorbed aggregates from the surface. It is thus not surprising that sliding the AFM probe across the surface at the described conditions exerts a torque on the cantilever that reflects the 5.3 nm periodicity of the adlayer, although we do not yet have a definite model to interpret this modulation –including the energetics of motion leading to the torque and the role of the hydrodynamics in the healing rates.

This imaging behavior also allows us to assess the temporal behavior of the surface aggregates. Since the spacing of two subsequent scan lines in Fig. 17c is only 78 pm, the tip essentially samples the area from which aggregates had been removed during the preceding scan line – a stripe roughly 9 nm of width. Since the micellar surfactant pattern is still detected in every scan line, the tip-induced defects must recover within the time between two subsequent scan lines. These patterns stay identical in shape and modulation height when the line frequency is varied between 5 and 60 Hz. This shows that (i) recovery occurs in the time between two scan lines and that (ii) complete, flawless recovery of the crystalline array of hemi-cylindrical micelles is achieved, even at the highest line frequency of 60 Hz. Thorough analysis of the tip trajectory

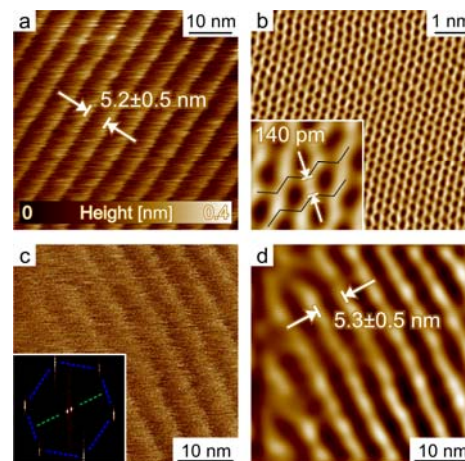


Figure 17. AFM images of surfactant aggregates on graphite. (a) Low-force topography image. (b) Small, high-force friction image, showing the graphite lattice only. (c) Larger, high-force friction image, showing aggregates and lattice simultaneously. Inset: Fourier transform. The blue and green lines highlight the orientation of lattice and micelles, respectively. (d) Band-pass filtered version of (c).

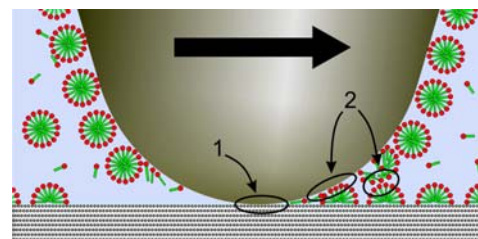


Figure 18. Schematic of AFM tip at high force, simultaneously touching the substrate at contact area “1” as well as the micellar aggregates at potential contact areas “2”.

allows us to conclude that this recovery is complete within ~ 6 ms.

In bulk SDS solutions, where the transport-limited $\tau_{1,bulk}$ is ~ 20 μ s, the formation of a bulk micelle, $\tau_{2,bulk}$ takes as long as ~ 2 ms. On surfaces, the previously measured diffusion rates of 10^{-12} to 10^{-10} m^2/s would allow to close a 20 nm diameter hole within a few microseconds. Similar to the bulk solution, we expect the self-assembly time of a surface micelle to be longer; our measurements show that the upper limit for this process is ~ 6 ms. On silica surfaces, adsorption and desorption times of surfactants are as long as seconds, which may indicate that the reorganization process described here is mainly due to redistribution of surfactant molecules on the surface rather than the exchange of the surfactants between the bulk liquid and the surface.

We have demonstrated that nanometer-scale defects in a crystalline array of surfactant surface micelles cure within 6 ms. Simultaneous imaging of both the substrate and the adsorbed layer of surfactant aggregates is achieved by monitoring friction forces while scanning in contact with the substrate. We thus acquire images at two ‘heights’, exhibiting features at the micellar and atomic length scales that are almost two orders of magnitude apart. We expect this technique to be of use not only in the study of the dynamic behavior of surfactant aggregates but with other adsorbed layers that exhibit a characteristic structural signature.

Self-Healing Coatings of Ionic Surfactant Micelles

Using liquid-cell atomic force microscopy (AFM), we demonstrated that ionic surfactants are capable of forming molecularly thin, self-healing layers on an atomically smooth, model surface. This is very promising for many applications such as corrosion inhibition, colloidal stabilization, and lubrication. Engineering surfaces that are used in most of these applications, however, are usually not atomically smooth. In order to be able to image surfactant aggregates on rough surfaces we use recently developed, soft AFM cantilevers with very sharp tips. Artifacts due to the size and shape of the tip that previously prevented micellar resolution on rough surfaces are hence greatly reduced. Using these probes we investigate aggregates of sodium dodecyl sulfate (SDS) surfactant on gold surfaces. Gold substrates can be rendered rough or atomically flat, thus enabling us to compare the role of surface roughness while keeping all other parameters fixed.

Applying the sharp AFM tips to image surfactant aggregates on rough surfaces we achieved a breakthrough. As the deflection image in a 10 mM SDS solution (Fig. 19a) shows, the entire gold surface is indeed covered with micellar surface aggregates. The geometry of each surface micelle is clearly revealed: The micelles are wormlike, featuring similar diameters of 5–9 nm, but a large variety of lengths. In comparison to the AFM images acquired on smooth gold, the micelles on rough gold surfaces display very different micelle morphologies. The micelles on smooth gold are very long, parallel. On rough gold, in contrast, they are quite curved and exhibit a considerable range of lengths. The shortest ones are of almost hemispherical shape; the larger ones more than 50 nm in length. We observe that the longer micelles on top of larger grains display a rather flat topography; while the shorter ones are located on small grains that are curved more strongly. A definitive relation to the gold lattice structure is not yet established.

To analyze these images more quantitatively, we computed a color-coded surface curvature map (Fig. 19b) of the area shown in Fig. 19a. We first applied a low-pass filter to the corresponding topography data to suppress features of micellar size or smaller; then, we calculated the mean curvature κ at each point. The peak values correspond to radii of curvature $R = 1/\kappa$ of ± 20 nm, where we use negative

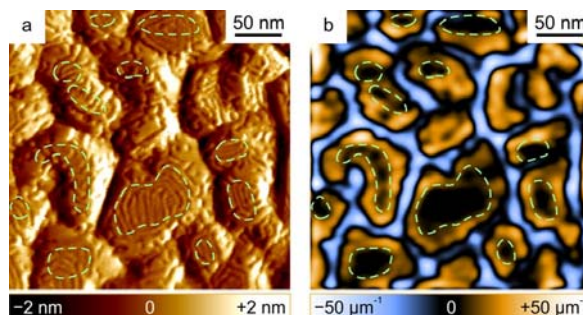


Figure 19: (a) AFM deflection image of surfactant aggregates on a rough gold film in contact with a 10 mM SDS solution taken with a sharp silicon AFM tip. (b) Calculated mean curvature of the surface shown in panel (a). Larger areas with low curvature (dark color) on top of the grains are highlighted by green, dashed lines. The same lines are shown in panel (a) to illustrate the correlation between low substrate curvature and elongated micelle morphology.

numbers/blue colors for concave areas (such as in the grooves between the grains), and positive numbers/ochre colors for convex areas (typically on the sides of the grains). The analysis confirms our observation expressed above: the larger areas of low curvature ($|\kappa| < 5 \mu\text{m}^{-1}$) on top of the grains (dark areas, highlighted by green, dashed lines) generally correlate with the areas that accommodate elongated micelles, while the brighter, ochre and blue areas typically host shorter or odd-shaped aggregates. One possible explanation for this behavior is that bending elongated micelles is energetically less favorable than forming several shorter micelles that are bent to a lesser degree. This is in line with the fact that we do not observe any micelles spanning two or more grains, which would also require a significant amount of bending due to the sample topography.

The aggregates of many commonly studied surfactants on smooth surfaces are close-packed micelles of cylindrical, hemicylindrical or spherical shape with typical center-to-center distances of 5–7 nm. We aim to estimate the influence of the size of the AFM probe on the obtained image of such samples, which proves relatively difficult. The micellar aggregates are soft structures that are removed from the surface by energies as little as 10–20 kJ/mol. The interactions between tip and sample are very complex and include electrostatic repulsion, van der Waals attraction, hydrophobic interactions and steric forces. Furthermore, the manufacturing process of AFM probes is subject to fluctuations, making their exact geometries at the nanometer scale unknown.

We use a much simplified, geometric model for our estimate, as illustrated in Fig. 20a. We idealize the tip by a sphere of radius r_T ; the micelles are simplified by identical hemicylinders or hemispheres of radius r_M , placed on a perfectly flat substrate. Further, we consider a gap of width g between the micelles, due to electrostatic repulsion between the head groups of the ionic surfactants. We assume that tip and micelles are incompressible and that the tip is in hard contact with the micelles while imaging. Consequently, the tip follows the wiggled, brown line in Fig. 20a, featuring a vertical modulation Δz as it slides across the micelle-covered surface. We further estimate the micelle radius r_M to be equal to the length of a fully stretched SDS molecule, $r_M = 1.9$ nm. Since we know that the center-to-center distance of SDS micelles is $d = 5.1$ nm in a 10 mM SDS solution, g is determined via the relationship $g = d - 2r_M = 1.3$ nm, a value that is backed by experimental evidence. Based on these assumptions, we computed the topography contrast Δz as a function of the tip radius r_T (brown curve in Fig. 20a). We assume no population of the anionic surfactant at the AFM tips which are made out of either silicon or silicon nitride (Si_3N_4). Both materials develop a negative surface charge in neutral pH as they form an oxide layer at the surface, so that repulsion between tip and surfactants is expected.

For a tip radius of 15 nm our model suggests a Δz of about 0.2 nm, slowly decreasing when the tip radius is increased (Fig. 10a). For tip radii of 10 nm and less, there is a relatively steep increase of the contrast as the tip radius is decreased. In the majority of previous AFM studies of these structures, Si_3N_4 cantilevers with tip radii of 20 nm and above were used. In this case a topography contrast of 0.1–0.2 nm

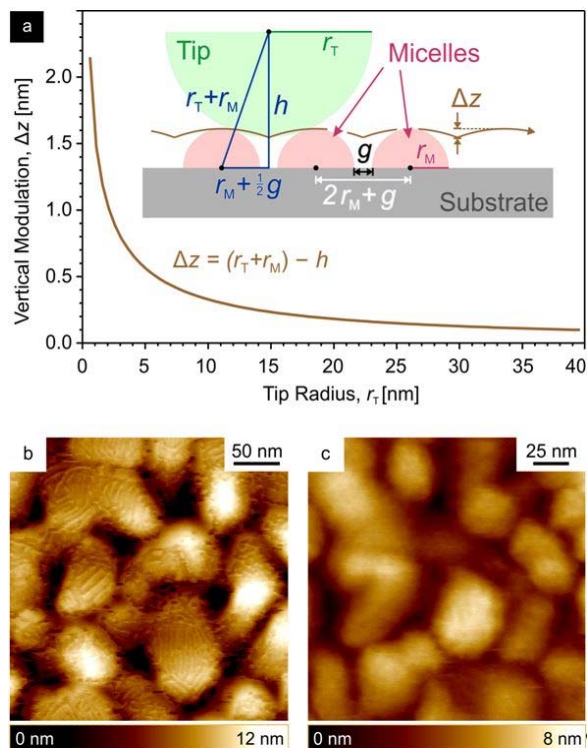


Figure 20: (a) When the AFM tip (idealized by a sphere of radius r_T) is larger than the imaged micelles (idealized by hemicylinders of radius r_M and with an intermittent gap of width g), the topography modulation is relatively small. By assuming that the tip is in hard contact with the sample and all bodies are incompressible, we can calculate the modulation Δz as a function of r_T , as shown in the plot ($r_M = 1.9$ nm, $g = 1.3$ nm). (b) Topography image of an evaporated gold film in a 10 mM SDS solution taken with a sharp AFM probe, featuring a high topography contrast. (c) When a Si_3Ni_4 tip is applied on a similar sample, the topography contrast is extremely weak.

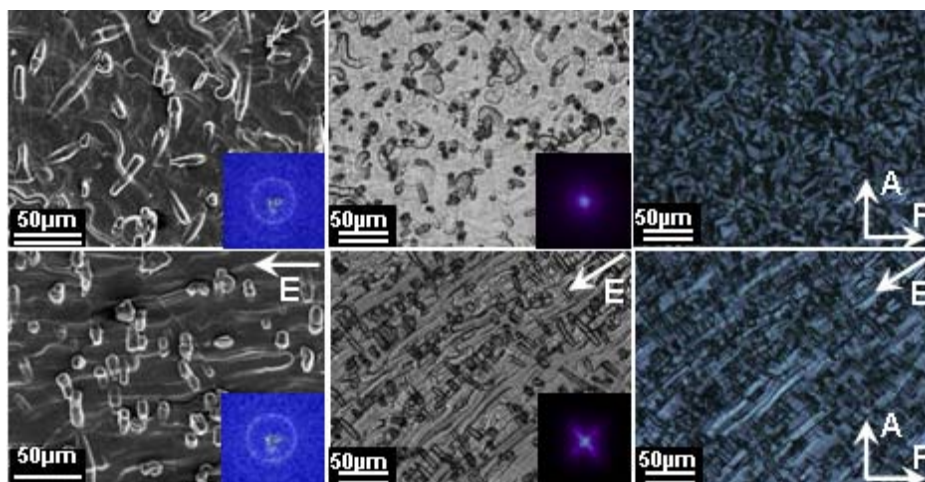


Figure 21: Scanning electron microscopy (SEM) images (left), optical microscopy (OM) images (middle), and polarized optical microscopy (POM) images (right) comparing control films (no field, top row) to films grown under electric fields (bottom row). Insets on left are small-angle x-ray scattering profiles; the E-field sample appears disordered due to the 3-D protrusions that grow out from the film. These protrusions appear to be the result of losing the 2-D confinement registry of the interface as the film grows thicker. Insets in the middle are Fourier transforms of the respective images; the two orientations in the E-field sample are a result of the protrusions being perpendicular to the field while the bulk film is parallel to the field.

was reported, in good agreement with our simple model. This topography contrast is small compared to other topographic features present in most samples, caused by defects in the substrate, non-planarity, sample tilt, and scanner bow. Using the sharp silicon probes, we achieve a much higher contrast that allows us to directly show the topography information, avoiding the difficulties associated with the deflection images. Fig. 20b shows that the micelle-induced topography contrast is even high enough to visualize the surfactant aggregates in a topography image taken on a rough surface with a peak-to-peak topography of 12 nm. Our model predicts a topography contrast of about 0.6 nm for the sharp tips ($r_T = 5$ nm). This is what we see in some cases (Fig. 19a); in other cases (Fig. 20b) we obtain a topography contrast up to 1.2 nm. This discrepancy is either due to our oversimplified model, or it is because some tips are sharper than specified. According to our model, the observed topography contrast of 1.2 nm would be reached with a tip radius of about 2 nm. Topography images of surfactant aggregates on rough surfaces taken with a Si_3N_4 tip, in contrast, are essentially useless: the topography contrast induced by the surfactant aggregates is negligible with respect to the topography of the rough substrate; the micelles are invisible in the topography signal (Fig. 20c).

Electric Field-Guided Growth of Mesoscopic Silica Thin Films

We studied the effect of low strength electric fields on mesoscopic silica formed from combining an acidified (0.49M HCl) cetyltrimethylammonium chloride (CTAC) micellar solution with the silicon alkoxide tetraethoxysilane (TEOS). Once mixed, particles and thin films spontaneously grow in the bulk solution and at all interfaces, respectively. The final particles and films consist of hexagonally packed surfactant tubules encased in a silica matrix. The surfactant can be removed, leaving behind mesoporous silica. Our work has focused on thin films grown at the air-water interface since they are continuous, large area, and easily adapted as they are free-standing. However, while having well-defined short range order, mesoscopic silica thin films exhibit very poor long range mesophase orientational order that would enhance pore accessibility in the final mesoporous silica.

Previously, our group demonstrated that weak electric fields ($\sim 100\text{V/m}$) can be used to merge and orient discrete mesoscopic silica thin films at solid liquid interfaces with the surfactant tubules parallel to the field lines. As shown in Figure 10, we can also achieve orientations in free standing, continuous thin films on the micrometer length scale over large areas ($\sim 60\text{cm}^2$) using even weaker electric fields ($\sim 3\text{V/m}$). The POM images in Figure 21 suggest nanometer orientation parallel to the field lines. Orientation of the nanometer-level structure was confirmed via transmission electron microscopy

(TEM), as shown in Figure 21. In addition, it was found that orientation only occurred when the electrodes pierced the film. Placing the electrodes underneath, but not piercing, the film resulted in films that displayed morphologies nearly identical to control samples. This means that the orientation comes as a result of the field acting on charge *within* the film.

THEORETICAL MODELING

Contact Charge Separation

The affinity of the hydroxide toward the hydrophobic surface is expected to play an important role in tribocharging of hydrophobic polymers. We have investigated the propensity of H^+ and OH^- water ions to reside near hydrophobic interfaces. Specifically, we have carried out initial first principles molecular dynamics simulations for applicable model systems. In these models, H^+ and OH^- water ions were placed within a slab of water near the opposite hydrophobic walls (56 waters total). For computational efficiency, a hydrogenated graphene sheet was chosen to represent a model hydrophobic surface. These simulations have revealed that larger simulation cells need to be employed for higher reliability. In this reporting period, we have done first principles simulations for larger systems, focusing on the dynamics of the ions in the course of simulations, and possible driving forces behind the ions' affinity toward hydrophobic surfaces.

The hydrophobic interface was represented by a 6x6 hydrogenated graphite supercell (72 C and 32 H atoms), which should be compared to 4x4 supercell in the earlier simulations. The water slab contained 126 water molecules, and a pair of H_3O^+ and OH^- ions. Fig. 22A depicts the overall geometry of the model system, with the ions near the opposite interfaces marked in blue. Fig. 22B shows the evolution of the vertical position of the hydroxide and of the hydronium oxygen, O_{OH^-} and $O_{H_3O^+}$, respectively. Remarkably, both the hydrogen of OH^- (green line in Fig. 22B), and the non-bonded lone pair of $O_{H_3O^+}$ (red line in the same figure) always point toward the hydrophobic surface when the respective ions reside in the surface layer. This strict correlation is highly local, and disappears when the ions quit the layer of water molecules adjacent to the hydrophobic sheet.

A representative configuration of the interfacial OH^- is shown in Fig. 23A. The solvated complex resembles a distorted tetragonal pyramid with the hydrogen of OH^- facing the hydrophobic surface. During the two trajectories in Fig. 23B OH^- stayed for ~10 ps in the interfacial layer and spent the remaining time in the closest subsurface layer. At the interface proton jumps from neighboring surface molecules to this OH^- are approximately twice as frequent as proton jumps from subsurface water.

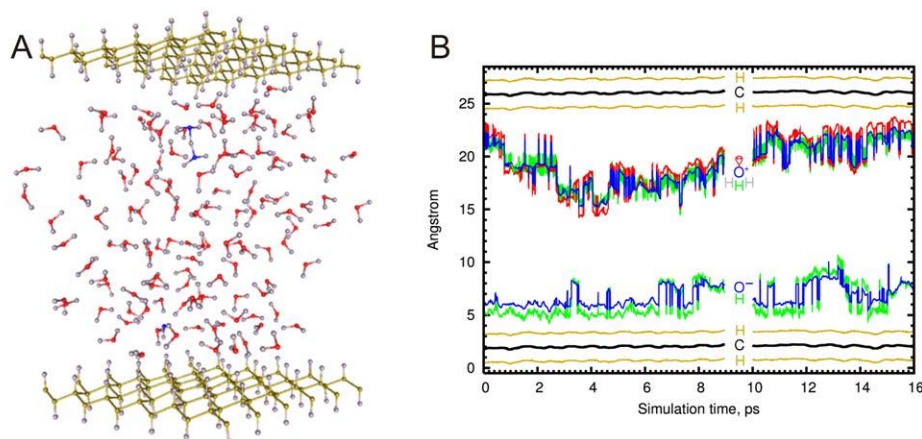


Figure 22: (A) Computational cell used in the simulations of water ions within the water slab sandwiched between 2 hydrophobic surfaces. (B) Time evolution (blue line) of the vertical position of the hydroxide oxygen and of the hydronium oxygen. Two trajectories are shown, the second one starting at $t = 10$ ps.

In water, the hydronium (H^+) complex constantly fluctuates between the so called Eigen H_3O^+ and Zundel $H_5O_2^+$ forms, due to fast proton exchange processes. In Fig. 23B we report a representative configuration of the hydronium at the interface. Near the hydrophobic sheet, the hydronium is in its Zundel form involving surface and subsurface water, and the lone pair of O_{H^+} is facing the hydrophobic surface. In our simulation a fluctuating Zundel/Eigen complex near a planar hydrophobic interface typically involved surface and subsurface water. Frequent surface-subsurface jumps of the O_{H^+} center are evident in both trajectories in Fig. 22B. Overall H^+ remained at the interfacial layer for ~ 7 ps.

To understand why the water ions orient themselves near a hydrophobic surface in such a way we developed a criterion to quantify the directional hydrogen bond (H-bond) affinity of a given chemical species M . This criterion is the projection of the electric field generated by M at the respective H-bonding site. The electric field projection is taken along the H-bond direction. In an H-bonded structure, this H-bonding site of M would be occupied by a neighboring molecule/ion forming a hydrogen bond with M . Specifically, for an H atom of M the probe site is where the lone pair of another molecule would be. Conversely, for a lone pair of M the probe site is where the H atom of another molecule would be. Given the predominantly electrostatic nature of the hydrogen bond, the magnitude of these electrostatic field projections is expected to be correlated with hydrogen bond strengths. Fig. 24 graphically represents this criterion for H_2O , H_3O^+ , and OH^- solvated species. The arrows begin at the probe sites, and are drawn in the directions of the electric field projections. The arrows' lengths represent the magnitude of the field. Judging by the magnitude of the electric field projections, in an H_2O the H and lone pair sides of the molecule are hydrophilic to a similar extent. On the other hand, the results for the ions are very different. The H side of OH^- and the lone pair side of H_3O^+ have small fields and are close in hydrophobicity to the H side of hydrogenated graphene (not shown). In contrast, the lone pair sides of OH^- and the H sides of H_3O^+ are strongly hydrophilic, even more so than the corresponding sides of the H_2O molecules. These observations clearly reveal the amphiphilic nature of the ions. Therefore, similarly to other surfactants, both OH^- and H^+ orient near a hydrophobic surface in such a way as to expose their hydrophobic sides to it.

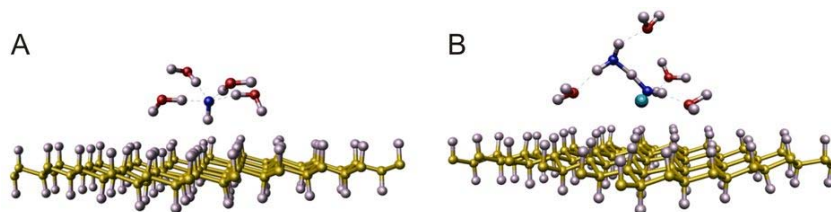


Figure 23: (A) Solvation structure of the hydroxide ion near the hydrophobic surface. Side view with the four solvating waters connected by broken lines to the oxygen of the hydroxide. (B) Solvation structure of the hydronium ion near the hydrophobic surface. Side view of a Zundel complex with surface and subsurface waters. The four solvating waters are connected to the outer hydrogens of the complex by broken lines. The lone electron pair is shown in cyan.

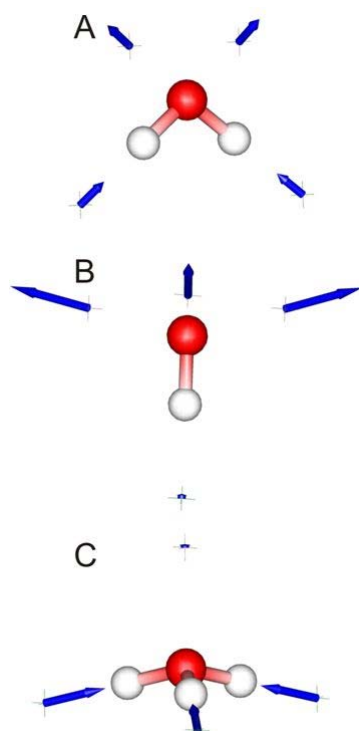


Figure 24: Electric field projections at probe points for (A) H_2O , (B) OH^- , (C) H_3O^+ . Note that as shown, the field vectors are fully 3-dimensional, and therefore their 2-dimensional length seen in the figure depends on how they are oriented with respect to the chosen point of view.

While due to the shortness of our present simulations we were unable to determine which of the two H^+ and OH^- ions has higher surface affinity, the preferences of the ions toward the water layer near a hydrophobic surface did emerge. Furthermore, the H^+ ion was often found to be delocalized between the surface and subsurface water layer due to its Zundel H_5O_2^+ , while OH^- firmly resided in the surface layer. This dynamical effect is a possible reason for the differences in surface affinity between OH^- and H^+ , as found in the zeta potential measurements.

We have also continued investigating the electrostatic properties of long oligomer chains. We established that when a charge transfer is transferred between the ends of such a long chain, the values of the acquired end charges are quantized. This finding provides an important insight into the charge transfer processes in various systems including push-pull polymers.

Charge Separation in Push-Pull Polymers

Push-pull polymers have received much attention due to their highly nonlinear electronic and optical responses. Such molecules usually contain a chain of atoms forming a conjugated π -electron system with electron donor and acceptor groups at the opposite ends. Upon electronic excitation a charge is transferred from the donor to the acceptor group, leading to remarkable nonlinear properties. What is surprising, however, is that nontrivial features already appear when addressing the lowest-order response of such molecules to the static electric fields, i.e., their dipole moment. A model push-pull polymer is shown in Figure 25. Note that instead of addressing computationally challenging excited states, we would rather much prefer to focus on the ground state properties. Therefore, in the case of the push-pull system shown in Figure 25, we have simulated the charge transfer not by moving an electron but by moving a proton from the COOH to NH_2 groups located at the opposite ends.

In our work we have investigated long but finite polymeric chains such as the push-pull polymer in Fig. 25, using the standard quantum chemistry (QC) approach. In particular, we considered the longitudinal dipole p and the end charges Q end of such systems. The main message of the present work is that the end charges, and the corresponding dipole of long polymeric chains, are quantized. Such quantization may look counterintuitive, being in sharp contrast with what happens in small molecules, where the dipole is *not quantized* and can assume any value. To the best of our knowledge, the quantization discussed here seems to be novel in the QC literature and in the theory of polymers at large. Nonetheless, the analogous phenomenon is well established in the physics of surfaces, where it goes under the name of “quantization of the surface charge.” A closely related theorem concerns the quantization of charge transport. The novelty of the present work in relation to the solid state physics literature is two-fold. First, the theorem is specialized to polymers and presented within the standard QC language and notation. Second, the proof of the theorem is based on quite different concepts and methods from previous studies.

The proof of the quantization theorem was carried out within the single-particle approach in the following steps: by mapping the finite and infinite quantum systems onto an equivalent system of point charges, by relating such finite and infinite systems to each other, and then by considering the most general finite system with arbitrary end groups. We believe that presenting the proof in this way illustrates the physical content of the theorem with greater detail. The case of a correlated wave function method is also mentioned, and while the quantization still holds, we do not prove it fully and only outline the steps necessary to reach such a conclusion. The actual effects of this quantization were studied in a toy LiF chain and functionalized oligomers of polyacetylene (Figure 26). In both cases, the asymptotic quantization is readily approached, with deviations of the order of 1.0×10^{-4} for the largest oligomers considered. One of the effects worth noting in the polyacetylene oligomers is that the dipole per monomer is uniquely determined only *modulo* the unit length a , i.e., the same identical unit cell (i.e., bulk) gives rise to numerically different dipole values. Such a *modulo a* arbitrariness always arises within the periodic Berry-phase approach as, for example, we have previously demonstrated. However, while in the periodic case, such arbitrariness may appear to be just a computational artifact of the Berry phases; here, we clearly see that, in fact, it corresponds to an actual physical effect that is observable in oligomer calculations. In general, the finite oligomer “chooses” one of the allowed quantized values, mandated by its bulk: which one depends on the chemical nature of the chain-end groups. Finally, by utilizing the localization argument, one could readily predict the dipole moments of relevant push-pull systems where the charge transfer takes place. There, one only has to identify the groups between which the charge transfer occurs, and the actual end charges become readily available by utilizing the proper sequence of steps.

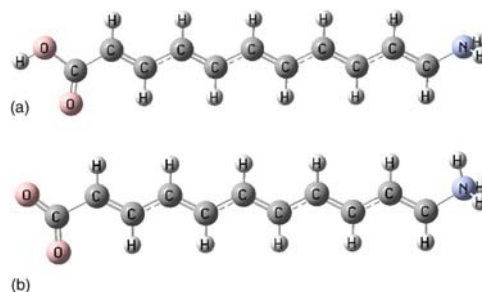


Figure 25: Two states of a prototypical push-pull system. The long insulating chain of alternant polyacetylene has a “donor” (NH₂) and “acceptor” (COOH) groups attached at the opposite ends. The charge transfer occurring in such systems upon some physical or chemical process is simulated here by moving a proton from the COOH to NH₂ groups: in (a) we show the “neutral” structure and in (b) the “charge-transfer” one. The two structures share the same “bulk,” where the cell (or repeating monomer) is C₂H₂, and the figure is drawn for $N_c=5$.

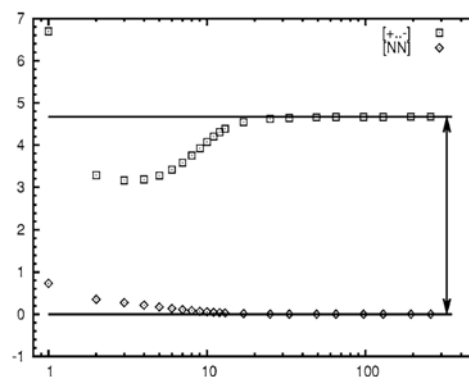


Figure 26: Longitudinal dipole moment per monomer $p(N_c)$ of the *trans*-polyacetylene oligomers, exemplified in Fig. 1, as a function of N_c : diamonds for the neutral structure [NN] [Fig. 1(a)] and squares for the charge transfer structure [+...-] [Fig. 1(b)]. The double arrow indicates their difference, which is exactly equal to one quantum.

Nanoscopically Confined Water

The properties of water confined in nanoscale geometries are of considerable scientific and technological interest. Nanoconfined water constitutes much of the environment in the cytoplasm of cells, where it acts as an active regulator of biological functions including protein folding.¹ Understanding the transport and thermodynamic properties of water in molecular-scale geometries is key in a wide array of fields, from nano- and microfluidics, to cloud seeding in the atmosphere, corrosion inhibition, and heterogeneous catalysis. Interesting phenomena arising in confined water have been observed experimentally, as well as in theoretical and computational studies. These include drastically different local structure and dynamics and the appearance of phase transitions not observable in the bulk under the same thermodynamic conditions. Such behavior arises from the subtle interplay of the fluid correlation and confinement geometric length scales and the nature of the interactions between water and the confining medium. Because confining surfaces modify the structure and dynamics of water, a fundamental understanding of the effect of confinement and the spatial range over which these effects are exerted are necessary.

In this study we use molecular dynamics (MD) simulations to investigate the effect of the confinement length scale on the local and average dynamics in a nanoscale water film at ambient conditions. We do this by characterizing the regions in which different dynamical properties deviate from the bulk value under the influence of the confining surfaces. We consider a thin water film confined between two rigid, hydrophilic silica surfaces mimicking the chemistry of hydroxylated β -cristobalite (Fig. 27). Periodic boundary conditions are imposed in the x and y directions, rendering the film macroscopic in the directions parallel to the surfaces. Confinement is imposed along the z -axis, normal to the surfaces, whose separation (d , the confinement length scale) is varied between 0.6 and 5.0 nm. We take d as the distance between the planes containing the hydrogen atoms of each surface. Our MD simulations in the canonical ensemble are equilibrated at 300 K and a mean density of $1.0 \text{ g}\cdot\text{cm}^{-3}$. Water-water interactions are modeled using the SPC/E pair potential, while water-surface interactions are treated using the potential by Lee and Rossky, which accounts for electrostatic and Lennard-Jones interactions between water and surface atoms.

Characterization is based on the local and average in-plane translational diffusion coefficient $D_{\parallel,\text{avg}}$ and the in-plane rotational relaxation time $\tau_{\parallel,\text{avg}}$. The latter term is computed by fitting a stretched exponential function to the dipole moment autocorrelation function. Fig. 28 presents these properties as a function of d . Fig. 8a shows that for all separations considered in our model, $D_{\parallel,\text{avg}}$ is smaller than that for bulk water (3.21×10^{-5}

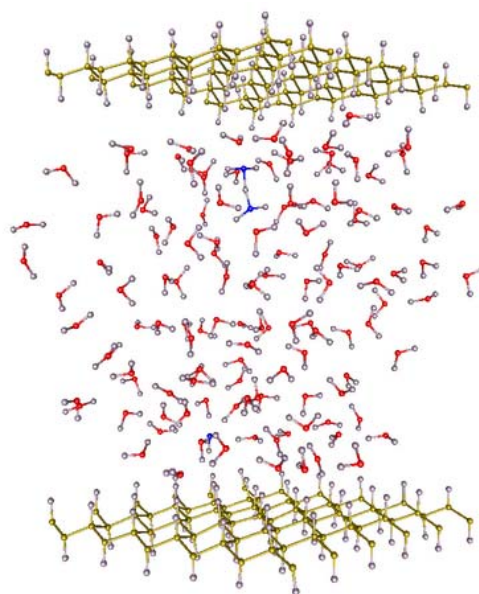


Figure 27. Computational cell used for water molecules between parallel hydrophobic surfaces.

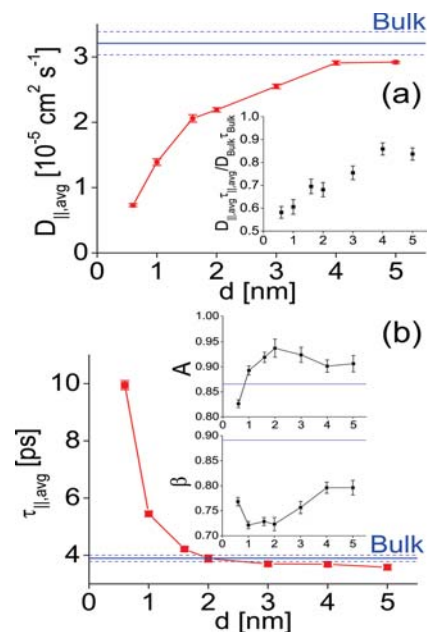


Figure 28: Average in-plane diffusion coefficient, $D_{\parallel,\text{avg}}$ (a), and rotational relaxation time, $\tau_{\parallel,\text{avg}}$ (b), as a function of confining surface separation, d . The inset in (a) presents the product of $D_{\parallel,\text{avg}}$ and $\tau_{\parallel,\text{avg}}$ normalized by the bulk properties as a function of d . Inset to (b): d dependence of the A and β parameters obtained from stretched exponential fits. Error estimates for D_{Bulk} and τ_{Bulk} are denoted by blue dashed lines. All data were obtained from MD simulations at $T = 300 \text{ K}$ and $\rho_{\text{avg}} = 1.0 \text{ g}\cdot\text{cm}^{-3}$. The x -axes in the three insets are values of d in nm.

DESIGN AND PROCESSING OF ELECTRET STRUCTURES

⁵ cm²·s⁻¹). On the other hand, Fig. 8b shows that $\tau_{||,avg}$ reaches bulk-like values when $d \geq 2.0$ nm. This decoupling of the translational diffusion from the rotational is a feature of supercooled liquids and has been observed in nanoconfined water. The presence of a confining surface results in anisotropic rotational motions since the OH or dipole may be hindered by water-substrate interactions. Evidence of anisotropic rotation of the dipole moment is seen in the decay of the in-plane dipole autocorrelation function (ACF) compared to the average out-of-plane ACF (not shown). At $t < 20$ ps, the rate of decay for both ADFs increases with d as expected for bulk-like water molecules (those nearest the center of the confined volume). While this trend continues for the in-plane ACF, the out-of-plane ACF exhibits a long tail, due to water-surface hydrogen bonding. Surprisingly, the absence of long-time correlations at $d = 0.6$ nm indicates that the hydrogen bonded network partially breaks down under severe confinement. This suggests that, as surface separation increases, water molecules near the surface form a more stable hydrogen bonded network that subsequently hinders out-of-plane rotations. This explains why the viscosity of confined water remains within a factor of three relative to bulk viscosity when held between mica surfaces to films one to two layers in thickness.
